THE ROLE OF FILM MORPHOLOGY AND DEFECTS ON THE PHOTOSTABILITY AND CARRIER TRANSPORT OF METHYLAMMONIUM LEAD TRIIODIDE

by

Jose Fernando Castaneda

A dissertation submitted to the faculty of
The University of North Carolina at Charlotte
in partial fulfillment of the requirements
for the degree of Doctor of Philosophy in
Nanoscale Science

Charlotte

2022

Approved by:

_____
Dr. Yong Zhang

_____
Dr. Abasifreke Ebong

_____
Dr. Juan Vivero-Escoto

_____
Dr. Thomas Schmedake

_____
Dr. Tsing-Hua Her

ABSTRACT

JOSE FERNANDO CASTANEDA. The Role of Film Morphology and Defects on the Photostability and Carrier Transport of Methylammonium Lead Triiodide
(Under the direction of DR. YONG ZHANG)

Organic-inorganic hybrid perovskites are viewed as a cost-effective alternative for photovoltaic devices, among other applications. Solution and low-temperature processing have gathered much attention for this class of materials. However, the stability and variability of reported fundamental properties have limited their progress toward practical applications. They suffer from environmental instabilities and undergo photochemical processes under light illumination that ultimately cause material degradation. The photostability of methylammonium lead triiodide ($MAPbI_3$) is probed by Raman spectroscopy, revealing that photodecomposition scales with surfaces and grain boundaries. Surface or defective regions are also shown to affect carrier transport properties and act as scattering centers for low-energy emitted photons. The disordered nature of $MAPbI_3$ and the additional structural defects of polycrystalline films result in restricted carrier diffusion lengths on the order of a micron determined by photoluminescence imaging, despite relative emission yields being much higher than an inorganic semiconductor like GaAs. In the literature, carrier diffusion lengths for $MAPbI_3$ have been significantly larger when determined by photocurrent measurements. However, conducting photoluminescence imaging on polycrystalline films under an applied bias illustrates that carrier diffusion is still relatively small. Carrier drift or the possible reabsorption of traveling low-energy photons reaching the perovskite/electrode interface can give a false impression of a much longer carrier diffusion within $MAPbI_3$.

DEDICATION

To my grandfather, always in our thoughts.

ACKNOWLEDGEMENTS

Over my time as a graduate student, I owe a lot to many. First and foremost, Dr. Yong Zhang for his guidance and direction. Always willing to provide feedback to my questions and with great patience. I owe a lot also to the environment within our research group. Many great peers whom I learned from. Liqin Su, Qiong Chen, and Jason Marmon welcomed me from the beginning. Taeyong Park for the many conceptual discussions. Fan Zhang, whom I collaborated with most. Tang Ye and Antardipan Pal for their support as we all aimed to complete our journeys within our programs. I fondly remember group meetings and hope new members will gain from learning from others as well. I owe much to the Nanoscale Science Program for the opportunities offered to students. During my time, I have been exposed to aspects of chemistry, physics, as well as electrical engineering. I also owe a great thank you to Dr. Bernadette Donovan-Merkert for her words of encouragement that lifted morale even at its lowest. I thank the faculty and members of my dissertation committee. Dr. Tsing-Hua Her and Dr. Juan Vivero-Escoto for their feedback and insight, stemming from my time as a chemistry student working towards a master's degree to now. I thank Dr. Thomas Schmedake and Dr. Abasifreke Ebong for their critique and feedback on the work conducted. This work was only possible with materials from various groups. Dr. Nam-Gyu Park and his lab at Sungkyunkwan University. Dr. Shengzhong Liu and his lab at Shaanxi Normal University. Dr. Jinsong Huang and his lab at the University of North Carolina at Chapel Hill. Dr. Zhaoning Song and Dr. Yanfa Yan at the University of Toledo. Lastly, I thank my wife and family for their unwavering support and belief, even when I lacked it.

TABLE OF CONTENTS

LIST OF FIGURES

CHAPTER 1: Introduction

1.1 Lead Halide Perovskites

Organic-inorganic hybrid perovskites (OIPs) are promising materials for applications such as solar cells, lasers, and light-emitting diodes.[1-3] Specifically, lead halide perovskites have gathered much focus over recent years, viewed as a cost-effective alternative for use in these optoelectronic applications. The most commonly studied methylammonium lead triiodide ($MAPbI_3$) is formed from common pre-cursors, solution-processable, and has demonstrated the tunability of its optoelectronic properties through routes such as introducing lighter halogens during synthesis.[4] This route has produced a material that has a tunable bandgap that can span most of the visible range. Hybrid perovskites notably have sparked the most interest in solar cells, as power-conversion efficiencies are comparable to the best inorganic PV devices available.[5] The impressive results in PV-related applications have often been attributed to large absorption coefficients, long-lived excited charges, and carrier diffusion lengths, all viewed as desirable properties.[6, 7]

1.2 Perovskite Structure

The lead halide perovskite structure follows ABX_3 stoichiometry, which consists of a 3D network of corner-sharing PbX_6 octahedra with cations such as methylammonium (MA) occupying the cavities or A site in each unit cell, as shown in Figure 1. The unique tunability within these materials arises through substituting the various atomic sites. The A site indirectly affects electronic properties and is essential for structural stability and formation.[8] The B and X site atoms directly contribute to the electronic bandgap of the material by forming the lowest conduction and highest valence

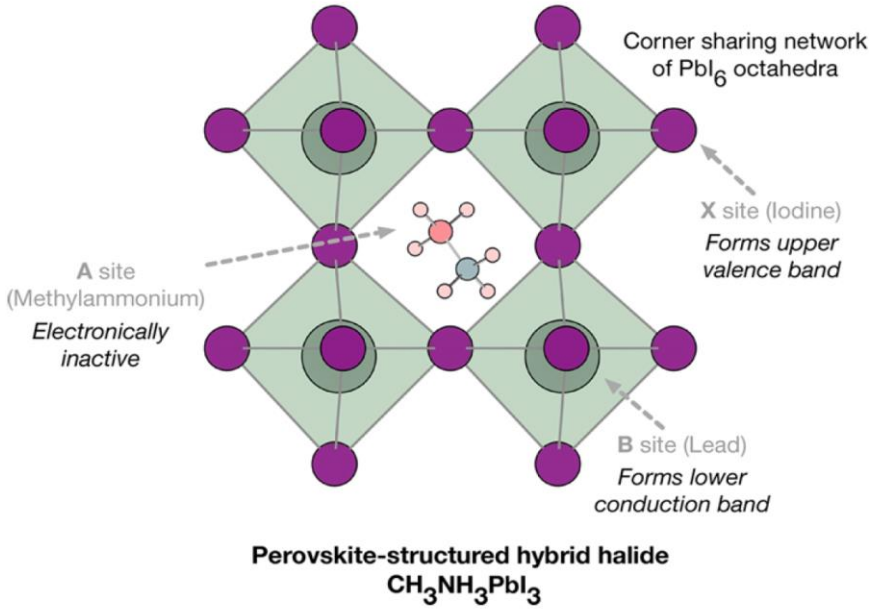

Figure 1. Methylammonium lead triiodide unit cell. Image from ref. 9.

bands, respectively.[9] The $MAPbI_3$ structure is dynamically disordered and undergoes various phase transitions as the temperature is increased from below 165 K to above 327 K.[10] In the lower temperature regime (<165 K), an orthorhombic phase is obtained where the MA ions become fully ordered and aligned in an alternating head-to-tail arrangement. In this phase, the strong H-bonding between the MA amine group and iodine distorts the lattice from the idealistic cubic perovskite structure. With increasing temperature (>165 K but < 327 K), the tetragonal phase transition occurs where H-bonding is weakened and lessens the distortion introduced in the orthorhombic phase. Dynamic disorder is also displayed as MA ions can rearrange themselves across various energetically equivalent orientations. In the final cubic phase (>327 K), MA is orientationally disordered and almost rotationally free, with H-bonding weakening even more. With the various fluctuating MA orientations and accompanied distortions of the lattice, the organic-inorganic hybrid perovskite structure is a dynamically disordered system at and above room temperature.[11, 12]

1.3 Defect Tolerance and Stability

The nature of the $MAPbI_3$ atomic structure gives rise to unique optoelectronic properties, such as a low concentration of deep-level trap states, despite its low-temperature solution processing and resulting polycrystalline nature in thin films.[13-15] The material is said to display defect tolerance,[16] where imperfections that arise from the low-temperature processing only result in energetic states within the valence and conduction bands and a material that retains proper functionality despite a significant density of defects. This defect tolerance has even garnered attention for these materials in space applications due to an increased radiation hardness above typical semiconductors like Si and GaAs.[17] However, despite this, stability remains an issue for practical application.

The long-term stability of the hybrid perovskite is one of their main limiting factors towards commercialization. The structure is thermodynamically unstable for $MAPbI_3$. Decomposition into methylammonium iodide and lead iodide is favorable, indicating an intrinsic instability within the structure, and analogs of mixed cation and halides are suggested to be more suitable for application.[18, 19] Much effort has gone towards compositional engineering for these materials, where the stability and performance are optimized by interchanging atoms within the structure.[20] This intrinsic decomposition for $MAPbI_3$ is kinetically slow; however, ambient conditions accelerate this process by collapsing or modifying the structure with moisture and oxygen.[21] Water can incorporate into the structure with the formation of a new hydrated product or catalyze decomposition by removing methylammonium iodide (MAI), resulting in the loss of optical properties and transformation to lead iodide (PbI_2), its main decomposition product. Thermal instabilities also arise due to the organic molecule's volatility, leaving

the structure even under a nitrogen environment at similar working device temperatures.[22] Upon illumination, the photoexcitation process can also result in instability as excited carriers interact with defects, resulting in photoinduced ion migration and eventual structural collapse.[23] Ion migration is prevalent among these materials, resulting in changing compositions like the local doping,[24] and measured changes in optoelectronic properties. One example is the J-V hysteresis observed in constructed devices, making repeatable measurements challenging.[25] Common in all these sources of instability is that they partly arise from defects, surfaces, or interfaces and, therefore, the probed material's physical characteristics. However, with various reported synthesis methods, the physical characteristics often vary from one report to another.[20] The literature has immensely investigated surface passivation and encapsulation methods to mitigate these defect or surface-related issues; however, they remain prevalent.

1.4 Charge Transport

For any electronic application, it is essential to understand how charges move within the active material. Upon photoexcitation of a semiconductor, a concentration of excited charges form where they can recombine either radiatively or nonradiatively. For $MAPbI_3$, nonradiative recombination is lessened due to the low concentration of deep-level trap states while reported excited-state lifetimes range from hundreds of nanoseconds to microseconds leaving charges with ample time to travel.[6, 7] Movement of charges can be directed by the concentration gradient that is formed upon excitation or by an applied or built-in electric field. The former is classified as diffusion, while the latter as drift. The parameters pertinent to the two processes are related to each other by the Einstein relation (1).[26]

$$D = \mu \frac{kT}{q} \quad (1)$$

The diffusion coefficient (D) can be seen to be proportional to both the mobility (μ) and temperature (T), while k and q are the Boltzmann constant and fundamental charge, respectively. These properties can further be extended with knowledge of the carrier lifetime (τ) to determine carrier diffusion length (L_d) with the use of (2).[27]

$$L_d = \sqrt{D\tau} \quad (2)$$

Transport properties play a direct role in device performance. For instance, the efficiency of a solar cell describes how well a device can produce current from light-generated charges. However, if these light-generated charges recombine before reaching the device's contacts for extraction, no current is generated. Therefore, reducing contributors to recombination and extending the lifetimes (and diffusion and drift lengths) of carriers within devices is essential to increase the probability of charge extraction and produce current. This correlation between longer photogenerated carrier lifetimes and increased efficiencies has been seen in organic-inorganic perovskites solar cells.[6] Stranks et al. demonstrated that small incorporation of Cl atoms into the $MAPbI_3$ structure during synthesis increased the excited-state lifetime from 9.6 ns (without Cl) to 272.7 ns and the diffusion length from ~100 nm (without Cl) to ~1 μm. Devices constructed also demonstrated an increase in power conversion efficiency from 4.2 % (without Cl) to 12.2 %, showing how an increased lifetime and diffusion length increases device performance. It is thought that adding Cl improved crystallinity and reduced defect density. However, reported transport properties for OIPs are still far lower than typical inorganic semiconductors with widely spread values, making it difficult to form strategies for optimization and determine their intrinsic limits. Variations have also been

attributed to compositional and physical differences between probed materials, the variety of electrical techniques used to characterize constructed devices, any errors induced by ion migration, as well the quality of electrical contacts used.[28, 29]

The deformable nature of the organic-inorganic lattice also has been hypothesized to affect charge carrier movement. Light-emitting field-effect transistors suggested carrier mobilities increase by two orders of magnitude from 298 K to 78 K from reduced phonon scattering (lattice vibrations).[30] This increase in mobility with decreasing temperature has been seen in typical inorganic semiconductors such as GaAs.[31] Temperature-dependent photoluminescence studies have also suggested that carrier scattering is attributed to LO phonons through the Fröhlich interaction, which has been known to occur in polar or ionic crystals.[32, 33] Also presented within the literature is the formation of large polarons upon excitation, where the electron (or hole) interacts with the electric field produced by the polarized local lattice ions. Zhu et al. suggest that this mechanism can explain the unique trends, such as long-lived excited charges, low recombination rates, slow hot carrier thermalization, and the modest mobilities reported.[34] Vibrational studies have suggested such a state may indeed form.[35, 36] However, other interpretations have come forward directly opposing the polaron interpretation, such as dynamic disorder, which involves the evolution of the structure that results in localizing charge carriers.[37] However, with widely varying reported properties, forming a consensus on what occurs within the structure is challenging.

1.5 Research Motivation and Objectives

The common theme that motivated this work is the apparent role defects, surfaces, and morphology have on the structural stability and transport properties of $MAPbI_3$,

despite the defect tolerance these classes of materials are said to demonstrate.[16] $MAPbI_3$ functions as a less complex model system, as opposed to the structures with a mixed composition of various cations and halides. The properties obtained from this prototype system could indicate what may occur in more complex but related structures. Surfaces and grain boundaries are regions of high defect density, and in $MAPbI_3$, these locations undergo direct attack from moisture. Moisture-induced degradation has already been found to scale with the surfaces, indicating their significant role in environmental stability.[38] However, what is alarming is the instability caused by photochemical reactions with defective regions.[23] For photovoltaic applications, photoexcitation is a must for the material. The surface's role in photodecomposition was probed with above bandgap excitation Raman spectroscopy (Chapter 3) by observing polycrystalline films of various domain sizes and single crystals.

Micro-Raman spectroscopy can probe a material's composition, crystallinity, and crystalline phase, as well as spatial and morphological information. Micro-Raman spectroscopy also offers a diffraction-limited excitation spot, which allows for probing minimal amounts of material and reducing long-term illumination on photosensitive structures as averaged spectra produced by sampling many sites with short integration times retain high signal-to-noise ratios. Above bandgap excitation Raman spectroscopy directly probes photoinduced structural changes by monitoring the vibrational spectrum. For $MAPbI_3$, spectra have widely varied, often with spectral features that resemble the main decomposition product lead iodide (PbI_2).[39-46] Previous work has shown that materials from different sources/synthesis methods undergo various stages of degradation under the same conditions.[47] To form a consistent view of the Raman spectrum for

$MAPbI_3$ at room temperature, the crystal size dependence was probed to indicate which spectral features are intrinsic or resulting from photodegradation.

Ion migration also occurs within the hybrid perovskite structure and is facilitated at defective regions like surfaces.[48] When these materials are under a bias, hysteresis is known to occur due to the migration of ions with charge carriers, further complicating such experiments.[29, 49] This complicates most transport characterization as they are mainly done under a bias and contribute to the wide range of values reported.[28] Photoluminescence quenching methods attempt to reduce this possibility with charges captured by an acceptor (quencher) with no applied bias instead of electrodes. However, carrier diffusion is modified when an acceptor site, such as a defect, is present.[50] To overcome this, an electrodeless photoluminescence (PL) imaging method is used to measure the photoexcited carrier diffusion (Chapter 4) of $MAPbI_3$.

Radiative recombination of photoexcited charge carriers occurring about the site of excitation on the microscale can be probed by capturing the emitted light using an optical camera (PL imaging). Images collected contain information on the material's carrier diffusion length (Ld) and alleviate the issues from electric field-based and PL quenching methods. For thin films, the obtained carrier emission intensity images can be modeled as a 2D system by a modified Bessel function from which the diffusion length is obtained by least-squares fitting.[51] $MAPbI_3$ formed by several different methods, and resulting morphologies are observed and compared with GaAs, a material thought to be similar in carrier properties and scattering processes.[28, 52] Along with these comparisons, misconceptions regarding actual carrier diffusion, carrier drift, and the laterally guided propagation of photoluminescence within $MAPbI_3$ are clarified with energy-dependent

photoluminescence imaging without an electric filed applied and reduced possibility of ion migration. The results are also compared with photocurrent measurements.

Chapter 2: Materials and Experimental Methods

2.1 Materials

Materials were not synthesized within our lab but were obtained through collaborators at other institutions. Perovskites were received under a vacuum with drying agents within the packaging and stored within a vacuum desiccator in the dark to reduce exposure to ambient conditions until measurement.

Several materials were measured throughout the studies conducted. In probing the photostability of $MAPbI_3$ (Chapter 3), polycrystalline thin films (~300 - 400 nm) of varying domain sizes (SKKU) were obtained from collaborators at Sungkyunkwan University.[53] These films were synthesized in the two-step process where a PbI_2 layer was first deposited onto a TiO_2-coated glass substrate. Then a varying MAI concentrated solution (in 2-propanol) was spin-coated and annealed at 100 ºC. The variable concentration of MAI dictated the final average domain size, which was determined by the intercept method[54] on micrographs obtained with a JEOL SEM w/EDAX. Also, within these photostability studies, millimeter-sized single crystals (SNU) from Shaanxi Normal University were probed and created by a seed growth method.[55] Seed crystals were grown from a precursor solution of MAI and PbI_2 dissolved within gamma-butyrolactone held at 100 ºC. Extracted seeds were then heated at 100 ºC within a fresh precursor solution, with this cycle repeated each time with a larger crystal used as the new seed until the desired size. For measurements, all single crystals were cleaved with a razor to expose a portion of the interior bulk as the surface to probe.

The transport studies (Chapter 4) involved materials from other sources. Collaborators at the University of North Carolina at Chapel Hill provided polycrystalline

thin films (~500 nm) formed by blade coating. The blade coating procedure involved applying an equal molar MAI and PbI_2 precursor solution (in N,N′-dimethylformamide) onto a preheated ITO glass substrate swiped with a glass blade to allow spreading of the solution, followed by annealing at 100 ºC.[56] This resulted in a nonuniform film (UNC-B) that was further passivated by dipping into a sulfate or phosphate-containing solution and annealing to convert the surface into a wide-bandgap lead oxysalt layer.[57] Also, uniform films (UNC-U) were formed by adding alkylamines within the precursor solution before blade coating.[58] Collaborators at the University of Toledo also provided PMMA passivated polycrystalline thin films[59] (~200 nm) with (TOL-G) and without (TOL) gold electrodes deposited and millimeter-sized single crystals (TOL-S). These polycrystalline films were formed from an MAI and lead acetate trihydrate precursor solution at a 3:1 molar ratio in N,N′-dimethylformamide which was spin-coated onto FTO-coated glass and annealed to create the film.[60] The other material studied within the transport characterization was a GaAs double-heterostructure (B2206) consisting of $Al_{0.4}Ga_{0.6}As/GaAs/Al_{0.4}Ga_{0.6}As$ with 1 μm GaAs and 30 nm $Al_{0.4}Ga_{0.6}As$ barriers grown by molecular beam epitaxy obtained from collaborators at Arizona State University.[61]

2.2 Experimental setup

The experimental setup involved a Horiba LabRAM HR800 confocal Raman microscope with a 1200 g/mm grating that allowed for other components to be coupled within the optical path. An external 532 nm continuous wave laser was coupled into the microscope and used as the excitation source for all studies. This excitation energy reduces the potential for high-energy damage. It was also far from the photoluminescence signal for all materials that would interfere with the Raman spectroscopy measurement.

Figure 2 shows the experimental scheme, and upon entering the optical path, laser excitation (light blue) would be directed towards a laser rejection filter being either a 532 nm longpass or a 532 nm ultra-low frequency notch filter that further led the laser towards an objective lens that was focused onto the material being measured. In the photostability studies (Chapter 3), a 100x (0.90 NA) lens was used for the polycrystalline films, and a 50x long working distance (0.5 NA) lens was used for evaluating single

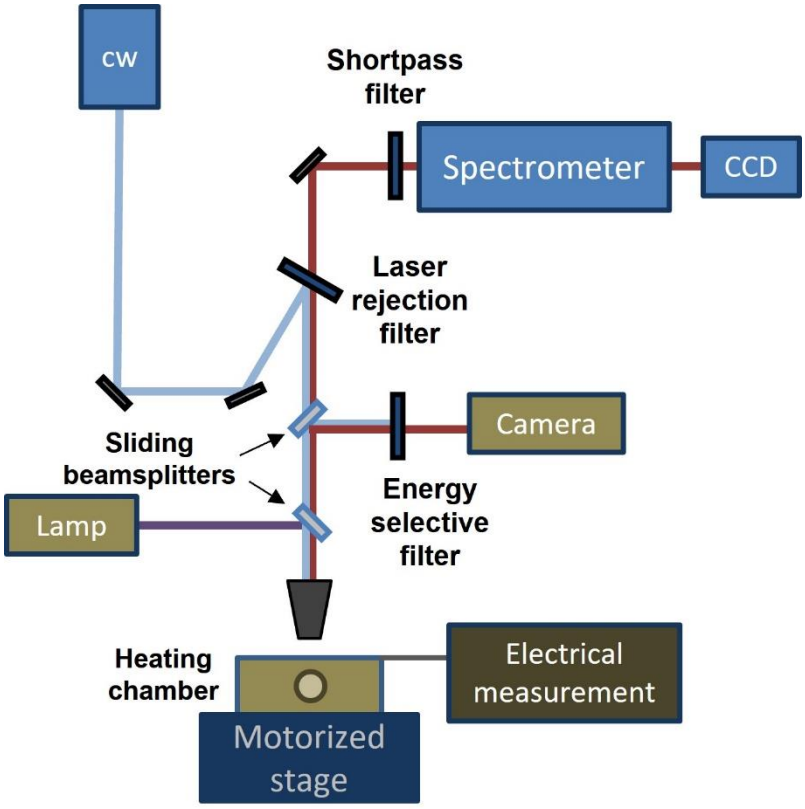

Figure 2. Experimental Setup

crystals. While for PL imaging, a 50x (0.95 NA) objective lens with chromatic correction was used. Below the objective lens, the material under measurement was either exposed to the ambient environment or placed within a Linkam TS1500 heating chamber for high-temperature measurements or a four-probe INSTEC HCP621GP stage coupled to a

Keithley 2401 source meter for applying a bias. The motorized stage upon which these components sat was run by a step motor that allowed raster scan spatial mapping.

Raman scattered or emitted photons (red) was captured by the same objective lens and directed towards the longpass or notch filter onward to the spectrometer and CCD for either photoluminescence or Raman spectroscopy measurements. Sliding beamsplitters could also redirect the collected signal toward the UI-2340SE-C-HQ (12-bit) optical camera for photoluminescence imaging.

2.3 Micro-Raman Spectroscopy

The photostability of $MAPbI_3$ was evaluated using micro-Raman spatial maps of 121 locations under 10 second focused excitation with a 100x (0.90 NA) objective lens and a 100 μm confocal hole. Excitation power densities (D) were calculated assuming a diffraction-limited spot size with D = P/A, where P is the laser power and A the area of the laser spot determined by 1.22(λex/NA). The excitation power, wavelength (λex), and the objective lens's numerical aperture (NA) determine the effective power density. Maps were collected to increase signal-to-noise and control the amount of light exposure to a single site by averaging all spectra to produce an average Raman spectrum.

Also, due to the high PL efficiencies of the hybrid perovskite,[15] a significant background signal arose from photoluminescence that exceeded the stray light suppression of the spectrometer, which would not occur for a typical inorganic semiconductor, such as GaAs, under the comparable excitation condition. This noise was reported in earlier work[47] and required a 650 nm shortpass filter placed before the confocal hole entrance of the spectrometer.[62] Figure 3 demonstrates this noise with and without the 650 nm shortpass filter on the spectrum obtained for a $MAPbI_3$

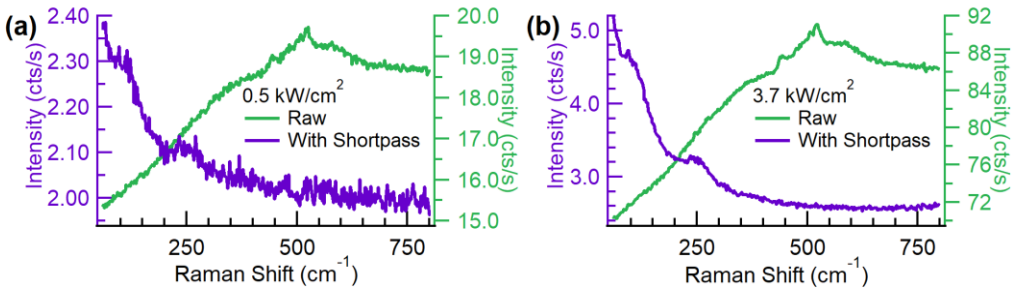

Figure 3. $MAPbI_3$ Raman spectra with and without the 650 nm shortpass in place at (a) 0.5 kW/cm^2 and (b) 3.7 kW/cm^2.

polycrystalline film with strong photoluminescence background. The raw signal (green) is broad, almost identical, and covers a wide range for the two excitation power densities. However, with the 650 nm shortpass filter (purple) in place, all photoluminescence is eliminated from reaching the spectrometer. The two broad Raman bands (~100 and ~250 cm^{-1}) of the perovskite structure are now visible but were not discernable in the raw spectrum. Due to the large discrepancy between the actual Raman scattered signal and the photoluminescence noise intensity, the spectra collected in their raw form reduced the ability to discern any small changes within the structure, as indicated by the two spectra displayed in Figures 3a and 3b. Along with spatial maps, time maps on a single location were also collected to evaluate the time-dependent changes to the $MAPbI_3$ Raman spectrum in the polycrystalline and single crystalline materials under continuous 2.5 second integration.

The temperature dependence of $MAPbI_3$ was measured within the Linkam TS1500 system with water flowing to cool the chamber. Applied heating was allowed to stabilize for 2 minutes before measurement. Laser excitation within this chamber occurs through a quartz window; however, this window distorts the focused excitation spot and affects the effective excitation power density. The effective density is likely lower than

the calculated value assuming a diffraction-limited spot size as the laser beam size appears to broaden. Optical images are shown in Figures 4a and 4b as the laser excitation is focused without and with passing through the quartz window of the heating chamber, respectively. Apparent is a broadening and distortion of the laser spot, essentially modifying the excitation area. This is further shown graphically with the average radial profile of the laser excitation in Figure 4c. The half-width half-maximum is nearly the

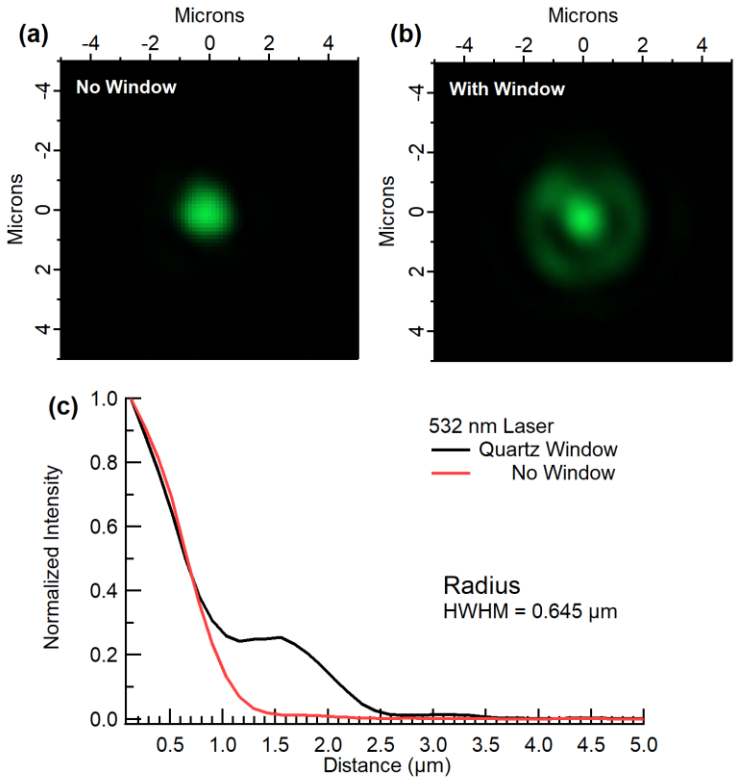

Figure 4. 532 nm laser profile imaged (a) without and (b) with quartz window and (c) average radial profiles.

same and in close agreement with the value determined by assuming a diffraction-limited spot; however, a widening occurs below half intensity when the quartz window is in place, most likely resulting in a lower effective excitation density than calculated. This distortion makes the actual value challenging to obtain and requires more evaluation to arrive at a more accurate assessment of the excitation density within the heating chamber.

The $MAPbI_3$ Raman spectrum also experienced notable baseline changes from contributions near 0 cm^{-1} from possible local polar fluctuations (Chapter 4) and the strong photoluminescence tail towards the higher wavenumber range (>600 cm^{-1}) at high excitation densities. Because of such changes in different portions of the spectrum, obtained Raman spectra were evaluated only from 60 - 425 cm^{-1} unless stated and underwent standard normal variate transformations to remove underlying baseline changes[63] and compare all spectra equally within this desired range.

2.4 Photoluminescence Spectroscopy and Imaging

Photoluminescence spectroscopy was collected under a 0.1 second integration time and 70 μm hole. Due to the probed materials' strong emission properties, CCD saturation quickly occurs at higher excitation powers, especially for the perovskite material. This was the shortest integration time possible within our system to allow the capture of the largest possible excitation range. Photoluminescence spectra to aid in evaluating the photostability (Chapter 3) of the $MAPbI_3$ thin films were obtained by the 100x (0.9 NA) objective lens.

For the transport studies (Chapter 4), a 50x (0.95 NA) lens with chromatic correction was used for both photoluminescence spectra collection and images captured with the optical camera. To calculate the excitation densities with this objective lens, the D = P/A equation was again used, except the spot area (A) was determined from the measured 516 nm half-width half-maximum of the laser profile as it deviated from the value specified by assuming a diffraction-limited spot. Films with gold electrodes were placed in the four-probe INSTEC HCP621GP stage and coupled to a Keithley 2401 source meter for applying a bias. To correlate the collected spectra and imaging results,

sliding beamsplitters were placed within the optical path to send the signal to the spectrometer and the optical camera. These beamsplitters also redirect the laser excitation, and selective filters were used to reject the laser contribution during imaging. For all materials measured, emission primarily arises at longer wavelengths (>650 nm), and a 633 nm longpass filter allowed laser excitation rejection and imaging of all emission counts. However, to selectively image specific energies within the photoluminescence band for $MAPbI_3$, 730 nm, 770 nm, and 810 nm bandpass filters were used, all with 10 nm bandwidths. Likewise, 870 nm and 890 nm bandpass filters were used to image specific energies within GaAs, all with 10 nm bandwidths. Image capture settings were set through the uEye cockpit under the IDS camera manager for the optical camera with frames per second set to 1.25 and exposure times adjusted to avoid pixel saturation using the pixel count histogram within the uEye cockpit. Captured images were corrected for dark counts by subtracting images collected in the dark through ImageJ. The Radial profile plugin within ImageJ was also used to produce average emission intensity profiles. The Image line profile function within IgorPro 6.37 was used to create line profiles from collected images.

CHAPTER 3: Photostability of $MAPbI_3$ Probed by Raman Spectroscopy

This chapter reused content in the article below.

3.1 Overview

Organic-inorganic hybrid perovskites (OIPs) suffer from several instabilities affecting long-term application and commercialization. Not only are environmental sources like heating[64, 65] and an ambient atmosphere[22, 38, 66] an issue, but the photoexcitation[23] process itself causes instability within this unique structure. Making trends and fundamental properties challenging to reach consensus due to variability even within contrasting synthesis methods used throughout the literature.[25]

Raman spectra of $MAPbI_3$ have widely varied with shifts of peaks as well as spectral features that resemble the main decomposition product PbI_2.[39-47] Conditions reported have been both in the resonant and nonresonant regimes, which could partially explain some of the discrepancies, as in the former excitation is absorbed to excite electronic transitions that generate charge carriers and can produce heating of the material if the excitation power is too high. Raman scattering in the resonant and nonresonant regimes also follow different selection rules, potentially affecting the spectrum's shape.[33]

Often lacking are the specifics regarding sample characterization for such measurements, like the crystal domain size in the case of polycrystalline films, which directly results from the specific synthesis method used. Previous work in our group

showed that materials from different sources/synthesis methods exposed to the same conditions undergo various degrees of degradation.[47] OIPs are also known to have low thermal conductivities with values more in line with what would be seen in organic semiconductors,[67] quite different from their inorganic counterparts to which they are often compared. Considering these various pieces of information, a systematic Raman spectroscopy study is needed to determine the intrinsic Raman spectrum of $MAPbI_3$. With this knowledge and the above bandgap excitation, the photostability of the structure can also be monitored.

3.2 Excitation Power-Dependence of $MAPbI_3$ Polycrystalline Films

The crystal size dependence under 532 nm laser excitation was probed to form a consistent view of the above bandgap excitation Raman spectrum of $MAPbI_3$ at room temperature. Exposing all sizes to the same conditions will indicate which trends are intrinsic or result due to structural changes. SEM micrographs of polycrystalline films (SKKU) with average crystal domain sizes of 0.4, 0.9, and 1.4 μm are shown in Figure 5. An excitation power-dependent study was conducted to evaluate the photostability by producing averaged spectra from 121 locations and using a short integration time (10 s) to increase the signal-to-noise ratio and minimize the long-term exposure at each site due to the strong photoabsorption of the material. The lowest excitation power density used produced Raman spectra consisting of two broad bands on top of a decreasing baseline, as shown in Figure 5.

The lack of sharp Raman peaks is understandable due to the known disorder in $MAPbI_3$ in its tetragonal phase at room temperature.[10, 12] The first band has been attributed to the inorganic portion of the lattice as these are Pb-I (~100 cm^{-1}) stretching

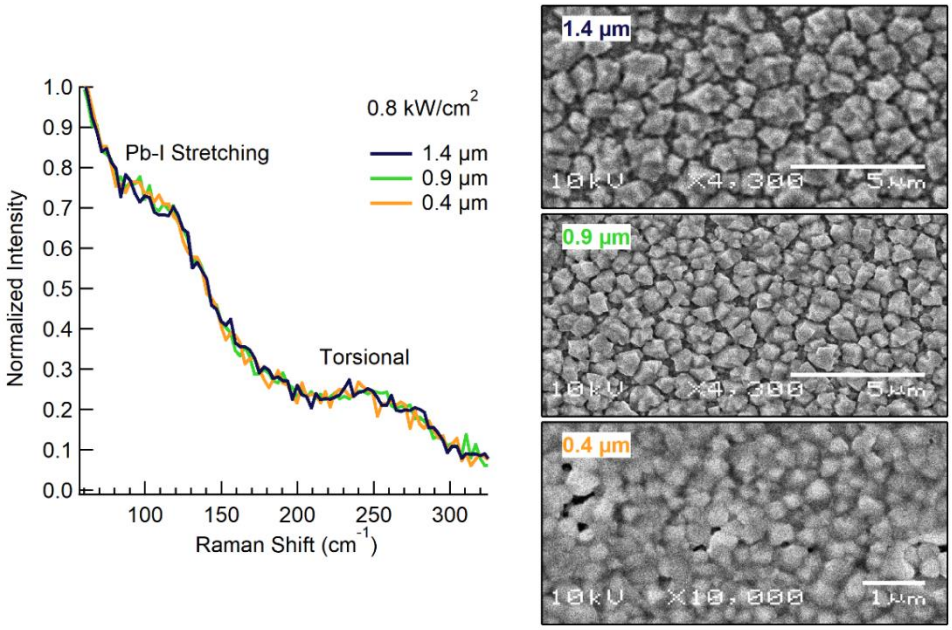

Figure 5. Raman spectra of polycrystalline films at 0.8 kW/cm^2 and SEM micrographs.

modes as calculated by DFT.[42] The second band (~250 cm^{-1}) is regarding rotation about the C-N bond in methylammonium (MA), which can be affected by the halogen due to hydrogen bonding[68] as well from deformation of the cavity[40, 44] that the MA ion resides within the octahedra network. The torsional mode has been suggested to be a measure of order and also sensitive to temperature.[42-44] The diffused baseline, decreasing from the laser frequency, is another manifestation of dynamic disorder within these materials.[37, 69, 70] It diminishes at lower temperatures, which also occurs in bromide and chloride analogs, as the rotational freedom of MA molecules is removed in the low-temperature orthorhombic phase.[70, 71] To ensure that the only variable changing is excitation power density, the collection time is fixed. It explains the noise level seen, especially at the lowest power density used, where the signal-to-noise ratio is expected to be the minimum. The three polycrystalline films in Figure 5 show very similar spectra (within the noise level) except at the Pb-I stretching band. The two smaller domain sizes have

slightly increased intensity levels, indicating slight structural differences compared to the largest size of 1.4 µm. These differences are relatively small compared to spectra within the literature for different domain sizes, as their variations were far more significant with several additional Raman peaks at 119 cm^{-1} and one ranging from 150 - 160 cm^{-1}.[44] As excitation power density increases, more considerable differences begin to occur and are summarized in Figure 6. Degradation occurs with the growth of 95 and 110 cm^{-1} peaks, which arise from the main decomposition product PbI_2,[47] and by monitoring the intensity

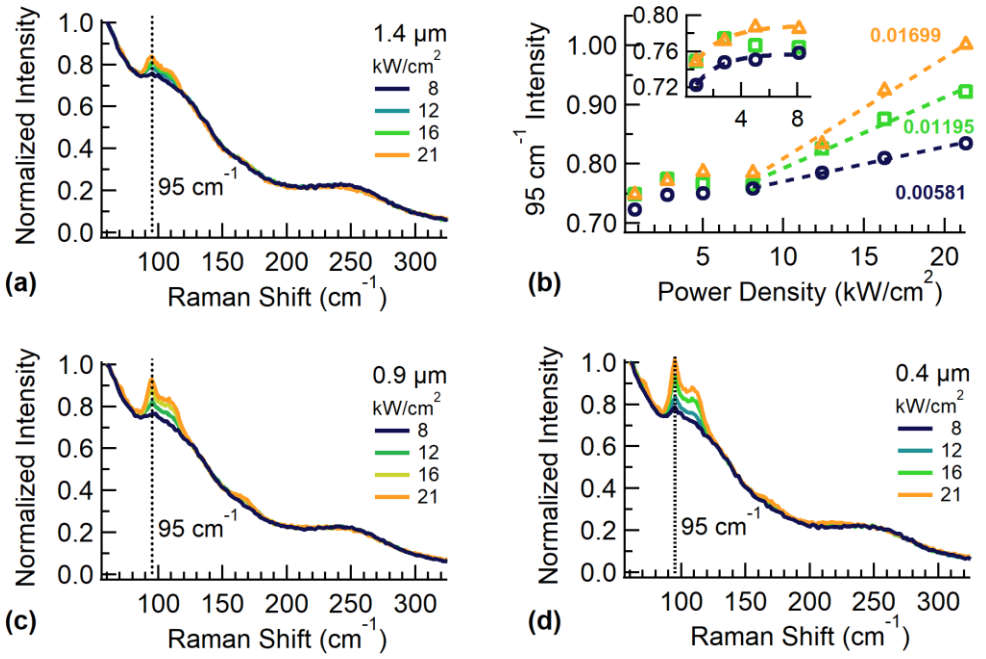

Figure 6. PbI_2 formation above 8 kW/cm^2 for (a) 1.4 µm, (c) 0.9 µm, and (d) 0.4 µm domain sizes along with (b) 95 cm^{-1} intensity growth with excitation power (inset: expanded low power region).

at 95 cm^{-1} for these averaged spectra (Figure 6b), the degradation process can then be tracked. Two regimes of structural change become apparent with increasing excitation power. In the low-power regime of 0.8 - 8 kW/cm^2, there is a slow increase that resembles a negative exponential function, as seen in the inset of Figure 6b; also apparent is that the intensity remains slightly higher as the domain size decreases. However, above

8 kW/cm^2, there appears to be a common threshold for all three films; above this threshold, the size dependence is more drastic as a rapid increase occurs.

In this high-power regime above 8 kW/cm^2, the 95 cm^{-1} intensity grows linearly with the 0.4 μm and 0.9 μm films, demonstrating ~3x and ~2x the growth rate of the 1.4 μm film. The 95 and 110 cm^{-1} peaks of PbI_2 from the high-power excitation are shown in Figures 6a, c, and d for all three films. Along with the growth of these prominent peaks, additional Raman modes of PbI_2[39] arise in the smaller domains at 70, 160, and 220 cm^{-1}, indicating extensive formation with increased excitation power.

Differences between the domain sizes arise primarily near the ~100 cm^{-1} band throughout the 0.8 - 21 kW/cm^2 power range. Throughout this range, the 95 cm^{-1} signal increases as the domain size decrease. The films measured here were made by the same synthesis method[53] resulting in their main difference being the final domain size. The resulting concentration of domains within the ~1 μm excitation beam (0.90 NA 100x objective lens) would then be different among these films, with the excitation spot size smaller than the average domain size of the 1.4 μm film. Still, several domains may be illuminated in the case of the smaller sizes. Due to this smaller size, more domains will be measured with a more surface-like environment, resulting in increased grain boundaries and probing photoreactive defects. Increased surface defects and grain boundaries imply more sites for the intercalation of H_2O[40] and O_2,[72] and known locations for charge carrier trapping and accumulation under photoexcitation.[23, 73, 74] All could lead to increased degradation rates in the smaller domain films.

Smaller domains could reduce thermal conductivity resulting in less efficient heat dissipation from laser illumination. However, the ultra-low thermal conductivities[67] of

these materials are similar to the intrinsic bulk value until below 100 nm.[75] If thermal conductivity differences dominated the photodegradation variations, the shared threshold between the low and high-power regions likely would not arise. At high excitation power, the 95 cm^{-1} signal scales linearly, suggesting that photoexcitation plays a more significant role, with the differences in linear rates between the domain sizes arising from the different contributions of the surface being probed. Kelvin force probe microscopy has shown that charges trap and accumulate along the grain boundaries under light soaking in $MAPbI_3$.[73] Along grain boundaries are a higher concentration of defects allowing for trapping to occur, which could yield in the deprotonation of MA[73] or from iodine-related

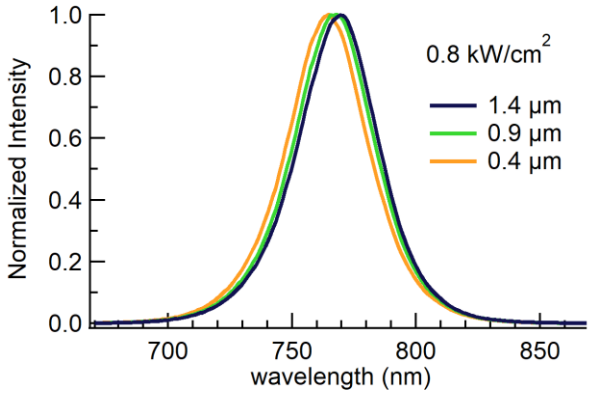

Figure 7. 0.8 kW/cm^2 averaged PL of polycrystalline films from 81 locations.

defects, which upon charge capture (hole or electron) can result in I_2. Both results cause degradation and collapse of the material as components of the structure are now mobile and able to escape or accumulate along the surface as ion migration is increased at defective interfaces.[23, 74] PL lineshapes in $MAPbI_3$ demonstrate that photoexcited carriers do not follow typical carrier thermalization as observed in conventional semiconductors such as GaAs. Instead, they tend to be more symmetric due to disorder and contain contributions from inhomogeneous independent regions.[15] Increased contributions from

the more defective surface can further affect obtained PL properties that reduce lifetimes,[23, 40] along with blueshifts that arise from the distorted structure in these regions,[40] as seen with obtained average PL spectra from 81 locations under 0.8 kW/cm^2 excitation (Figure 7), suggesting increased contributions from the surface as the domain size decreases.

3.3 High-Power Regime Kinetic Modeling of Polycrystalline Films

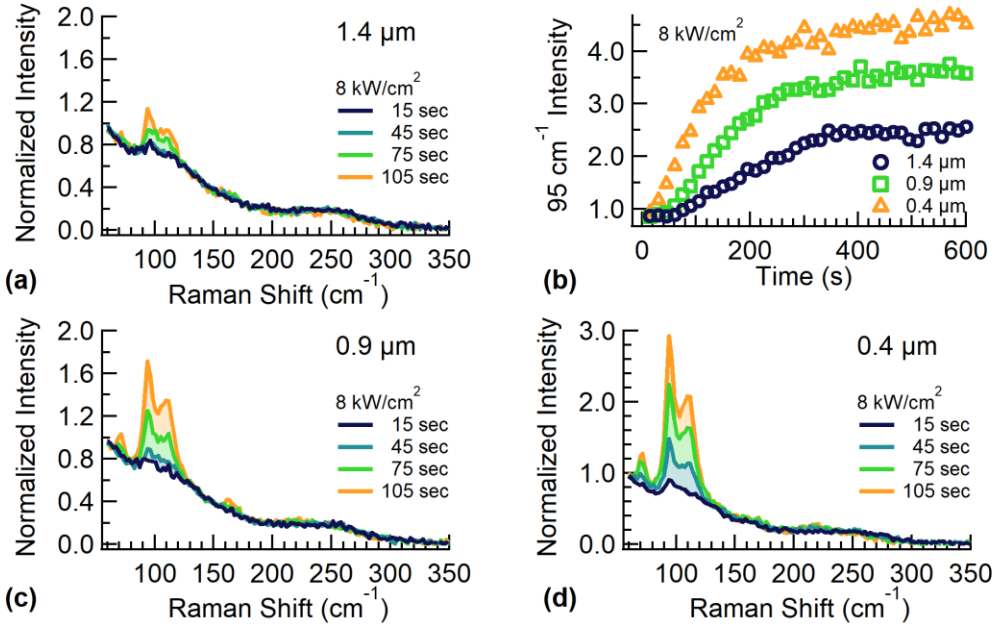

Figure 8. Early spectral changes under continuous illumination at 8 kW/cm^2 for (a) 1.4, (c) 0.9, and (d) 0.4 μm domain films; (b) 95 cm^{-1} intensity over time for all domain sizes.

In the low-power regime, spectra among the polycrystalline films vary to a small degree, mainly about the ~100 cm^{-1} band. However, PbI_2 forms linearly with excitation power in the high-power region at different rates. The transformation process was monitored over time at 8 kW/cm^2, the excitation power close to the stability threshold seen in Figure 6b. Spectral changes are taken from the average of 9 locations for each domain size, with the 95 cm^{-1} intensity used as the marker for PbI_2. Figures 8a, c, and d show several spectra collected initially within the transformation for all three films. In

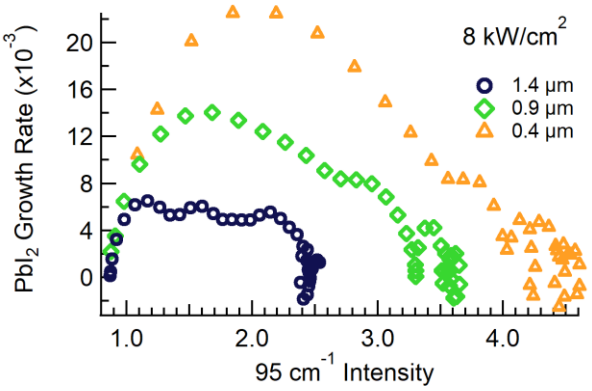

Figure 9. PbI_2 growth rate, dI(95 cm^{-1})/dt, as transformation reaches completion.

agreement with the power-dependent results from Figure 6, the growth of 70, 95, 110, 160, and 220 cm^{-1} peaks indicate extensive PbI_2 formation. Figure 8b shows that the 95 cm^{-1} intensity again differs between the three domain sizes, where PbI_2 forms more rapidly as the domain size decreases. The growth begins slowly before increasing, then falling again and plateauing as the process ends, producing a sigmoidal shape. This sigmoidal shape results from an increasing transformation rate that reaches a maximum, followed by slowing as the reaction comes to completion (Figure 9), indicating Avrami kinetics.[65, 76-79]

The Avrami model is used to describe the nucleation and growth of a new phase by (3)

$$\alpha = 1 - exp^{-kt^n} \quad (3)$$

where α is the transformed fraction, k is the effective reaction rate, and n is a parameter incorporating the new phase's variable nucleation rate and growth dimensions under isothermal conditions. Avrami kinetics have been used to describe several processes for OIPs, such as the formation and crystallization of the perovskite phase.[77, 78] Also, their degradation in constructed solar cells,[65] exposure to the ambient environment,[79] and X-

ray irradiation.[16] It is first customary to transform the signal (95 cm^{-1} intensity) into an α value determined by the starting initial value (S_0), value at time t (S_t), and the final value (S_f) at the end of the process, as shown in (4).

$$\alpha = \frac{S_0 - S_t}{S_0 - S_f} \tag{4}$$

Equation 3 can be rearranged to produce

$$\ln\left(-\ln(1-\alpha)\right) = n\ln(t) + \ln(k) \tag{5}$$

allowing determination of k and n by plotting the relationship between ln(-ln(1-α)) and

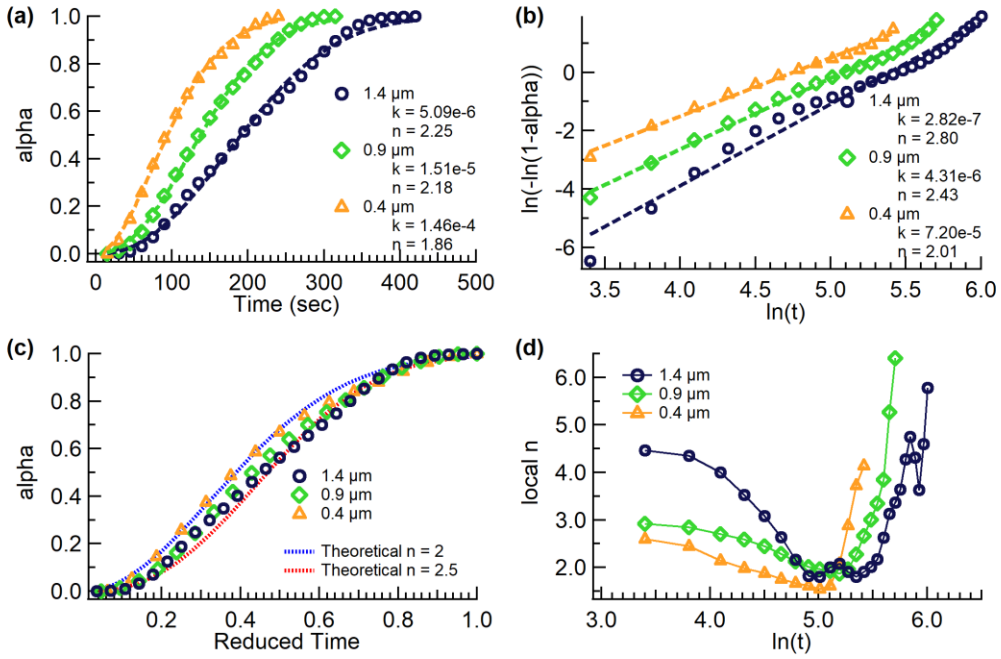

Figure 10. (a) Transformation over time, (b) Avrami Plot for all three domains, (c) Reduced-Time Plot, and (d) Local n changes over time.

ln(t).[80] Figures 10a and b use equations 3 and 5 to determine k and n, where long times have been removed due to increased noise after the reaction completion. In Figure 10a, α increases more rapidly over time as the domain size decreases, and fitting to (3), two trends occur where the reaction rate k increases and n decrease with decreasing domain size. In the Avrami plot, Figure 10b, formed by ln(-ln(1-α)) vs. ln(t), the k and n

parameters are determined from the slope of this relationship. Ideally, this relationship is linear. However, this is not the case indicating that the n parameters are not constant throughout the transformation process. However, linear fits have been applied to determine k and n for comparison with Figure 10a, indicating the same qualitative trend.

The Avrami parameter n provides mechanistic information, such as whether the nucleation rate is constant or already saturated when the transformation occurs. This parameter also incorporates how the new phase nuclei grow in spatial dimensions such as in 1D, 2D, or 3D.[81] The fluctuation and decrease of n indicate that the transformation mechanism is not constant over time. The new phase growth is further restricted in spatial dimension with a decreasing domain size. In Figure 10c, the transformation curves from Figure 10a are normalized to produce reduced-time (t/t_{α}) plots, where time is scaled by the time where α is ~0.99, and compared with theoretical curves calculated using the methods of Różycki and Maciejewski.[82] Reduced-time plots remove the differences between reaction rates and allow comparison on the same time scale, indicating that the transformation mechanism is different among the three domains where they appear to lie between the theoretical n = 2 (blue) and n = 2.5 (red) curves. If a shared mechanism were present, these curves would have overlapped.

Fluctuating n values have been a discussion within the literature. Reports indicate that they arise from assumptions breaking down within the Avrami model when applied to thin films or finite domains.[83, 84] Pang et al. have shown computationally that n is affected by the film thickness over time, monitoring what is called the local n throughout the transformation by (6).[83]

$$local\ n = \frac{d \ln [-\ln(1-\alpha)]}{d \ln (t)} \tag{6}$$

Surface nucleation beginning on one side of the film showed local n reduction as nuclei growth approached the opposite interior interface at small dimensions (thickness). However, the local n would decrease with larger sizes before eventually following 1D growth. This can be visualized as growing nuclei exhausting all available space laterally to each other before reaching the opposite interface and would form a plane that can only grow in one direction. This 1D plane growth was realized as a sharp increase in the local n at higher transformation fractions or later times. Figure 10d shows the local n for the three domain sizes versus ln(t). What is apparent is the decrease in the local n over time for all three domains before it increases dramatically, suggesting 1D growth is eventually reached during the reaction, and this process occurs earlier with smaller dimensions. Conceptually, this can be described by PbI_2 nuclei forming from the surface and growing in various dimensions before meeting each other and extending in the only available space in one direction. Providing an exact interpretation of these local n values at each specific time is difficult as additional measurements would be needed. However, qualitative trends could be alluded to by this analysis. Such as the relative difference in the local n at early times in Figure 10d. The larger 1.4 μm domain has a local n above 4, while the smaller domains are closer to 3. An increased local n could indicate more nonuniform nucleation as nuclei are more sparsely distributed over the surface. As a result, the local n is inflated as it grows faster than predicted.[83] This interpretation is qualitatively in agreement as less of the surface is measured in the 1.4 μm film.

3.4 Reduced Surface Contributions and Role of Temperature in Single Crystals

Polycrystalline films demonstrated that surfaces play a significant role in photodegradation, where defects initially form and grow inward in one direction as the

reaction proceeds. Single crystalline materials offer the opportunity to probe conditions where these surfaces play a reduced role. In polycrystalline films, surfaces are sites for charge carrier trapping and accumulation; however, this process is reduced in a single crystalline material from the decreased surface area. Furthermore, single crystalline structures have a well-defined surface, whereas a polycrystalline grain exhibits surfaces of different crystalline orientations, which might be different in environmental reactivity. Power-dependent spectral changes shown in Figure 11a (averaged over 600 s) demonstrate that PbI_2 formation requires relatively much higher excitation power (13.9 kW/cm^2) on a cleaved portion of a single crystal (SNU). Initially, there is very little

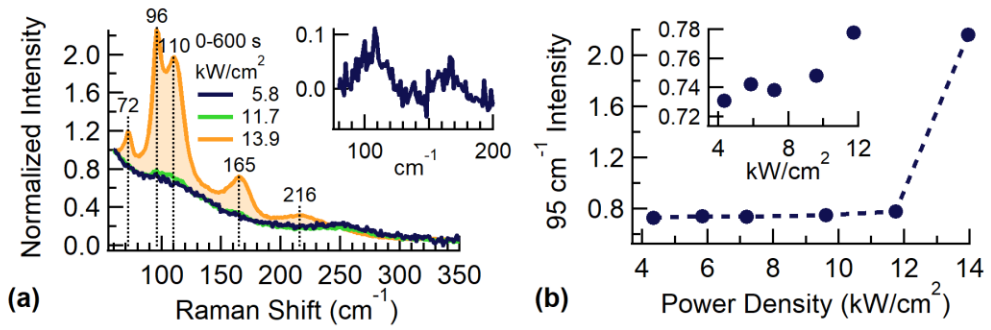

Figure 11. (a) Power-dependent spectral changes of a single crystal with excitation power (inset: different phase growth with two broad bands at ~110 and ~165 cm^{-1}) and (b) 95 cm^{-1} intensity change with excitation power (inset: expanded lower power region).

change as excitation power increases, as seen in the 95 cm^{-1} intensity in Figure 11b. This intensity increases slightly when reaching 11.7 kW/cm^2 (Figure 11b inset) before it becomes drastic at 13.9 kW/cm^2. However, this initial increase arises due to the growth of a different phase with broad peaks at ~110 and ~165 cm^{-1}. In subtracting curves from 11.7 and 5.8 kW/cm^2, these broad features are easier displayed (Figure 11a inset) and contribute to the increase in the 95 cm^{-1} intensity. As PbI_2 is formed at the highest excitation power (13.9 kW/cm^2), similar peaks to those in the polycrystalline films arise.

However, the relative intensities are different such as the ~165 cm^{-1} peak that is much higher.

Under photoexcitation, charge carrier generation, as well as heating, can occur. To probe the role of heating, spectral changes at excitation powers below the formation of PbI_2 were monitored at various temperatures within a heating chamber. Photoexcitation within this chamber is done through a quartz window and may introduce distortions of the laser profile and affect the actual excitation density on the material. The

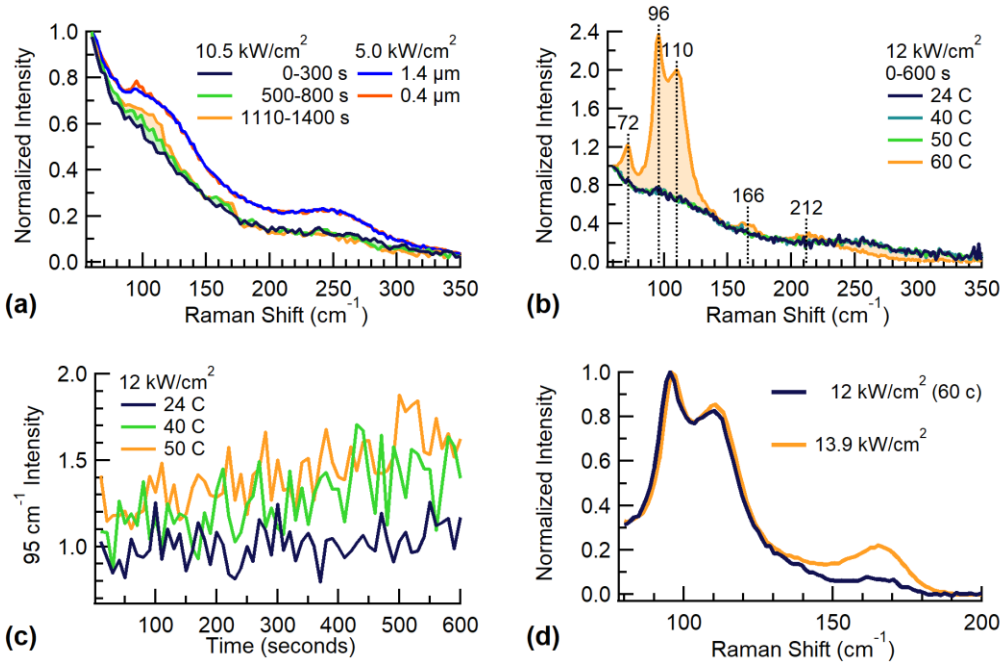

Figure 12. (a) Continuous illumination on single crystal at 20 ºC and comparison with polycrystalline thin films. (b) Temperature-dependent Raman spectra of a single crystal. (c) 95 cm^{-1} intensity over 600 seconds at different temperatures. (d) Spectral comparison between 12 kW/cm^2 at 60 ºC and high power 13.9 kW/cm^2.

following densities reported were calculated assuming a diffraction-limited spot size. Still, they may be higher than the actual densities on the material and need more evaluation to reach a more accurate assessment. The Raman spectrum on the same site was observed under continuous 2.5 second integration at 10.5 kW/cm^2. Figure 12a shows averaged spectra from this continuous monitoring at 20 ºC within three periods (0-300s,

500-800s, and 1100-1400s). In the first 300 seconds (dark blue), compared to spectra from the largest (blue) and smallest (red) domain films collected at a lower excitation power of 5.0 kW/cm^2, it is seen that the features are reduced in intensity within this spectral range with the ~100 and ~250 cm^{-1} broad bands suppressed. This decrease in spectral feature intensity was primarily seen in the single crystalline material but varied from location to location. A similar trend was reported when the Raman spectrum of a crystal face center was compared to the same crystal's more defective edge indicating that the strength of these broad features within the polycrystalline films may result from an imperfect surface being probed.[40] Nevertheless, progressively prolonged exposure to the excitation beam in the single crystal enhances the signal near ~110 cm^{-1} and ~160 cm^{-1} (green and orange traces in Figure 12a).

The formation of PbI_2, however, is only seen at higher applied temperatures. In Figure 12b, spectra collected from 24 ºC to 50 ºC, each over 600 seconds at a higher excitation of 12 kW/cm^2, are nearly identical, suggesting that heating is not the direct cause for PbI_2 formation under these excitation conditions. The 95 cm^{-1} intensity (without normalization) displayed in Figure 12c further shows that at 24 ºC, this intensity is relatively constant under laser excitation. However, with applied heating, this region increases from increases in the baseline at lower wavenumbers, further discussed in section 3.5, demonstrating that the applied heating has a more significant effect than potential heating from the laser excitation power. However, once 60 ºC is reached, features of PbI_2 become very prominent. This temperature is above the tetragonal to the cubic phase transition, around 54 ºC.[10] In this phase, it is suggested that the MA ion is less tightly bound due to the weakening of the hydrogen bonds that keep the molecule

within the cavity of the inorganic backbone structure. These results suggest that above the cubic phase transition, even the relatively more stable single-crystal system becomes less stable under photoexcitation, possibly facilitating ion migration and eventual structural collapse. Such combined heating and photoexcitation effects have also affected degradation in solar cell devices.[85] This finding is consistent with the understanding that $MAPbI_3$, despite having negative formation energy of the order of 0.1 eV (i.e., thermodynamically unstable),[19] a small kinetic barrier helps stabilize the structure in a relatively low-temperature range, which has led to developments in compositional engineering strategies toward more stable materials.[20] Such barrier may arise from the energy required for ion and defect migration that is also on the order of 0.1 eV for $MAPbI_3$.[86] This low formation energy plays an essential role in the stability of the material as seen in other work from our group where II-VI based organic-inorganic hybrid $ZnTe(en)_{0.5}$ demonstrated a much higher temperature and long term stability due to its sizable formation energy and kinetic barrier.[87]

However, the degraded spectra from the 60 ºC temperature increase (Figure 12b) and higher excitation at 13.9 kW/cm^2 (Figure 11a) resulted in slightly different shapes, as shown in Figure 12d. Spectral differences occur at ~110 and ~165 cm^{-1}. The difference at ~110 cm^{-1} is relatively small. However, the ~165 cm^{-1} is noticeably different under increased photoexcitation. The inset of Figure 11a showed that an additional phase grows under increasing excitation density with broad bands at ~110 and ~165 cm^{-1}. However, their reduced presence in the spectra at 60 ºC (Figure 12d) suggests that they are accompanied with the photoexcitation process. Peaks within this 100 – 200 cm^{-1} region have been suggested to be related to the libration modes of the MA ion from

calculations.[39, 42] However, they have also been reported to be defect associated with the possibility of oxygen incorporation, which was found in films deposited on substrates with varying properties.[72] In another study involving long-term excitation of polycrystalline films, it was also seen that these peaks arose later under illumination and were attributed to an I_x phase.[39] Exposure to high excitation also resulted in similar peaks for $MAPbI_3$ and other structures within the organic-inorganic perovskite family.[88] Polyiodides used to synthesize hybrid perovskites also reported similar peaks.[89] The fact that these peaks only appear after a longer illumination time (Figure 12a) or increasing excitation power (Figure 11a) indicates that we may attribute them to defect formation that results in an Iodine related species, most likely I_2 or I_3. An accumulation of iodine-related species on the surface under photoexcitation is thought to occur from charge traps and lead to additional defect generation with eventual saturation and PbI_2 formation.[23] A similar conclusion was made recently where two types of iodine-related defects were found in metal halide perovskite solar cells under bias and illumination.[74]

3.5 Structural Fluctuations Under Photoexcitation

The $MAPbI_3$ structure is a disordered system, as seen from the Raman spectra, with the rise of primarily broad bands at or above room temperature. Narrow features mainly arise when PbI_2, its main decomposition product, forms under external stimuli like light or heat. The MA ion is an asymmetric molecule that interacts with the inorganic lattice through hydrogen bonding but is dynamic as it tumbles and rotates within the cavity it sits within.[90] The lattice is also deformable, with active motion and large displacements. The large displacements within these classes of materials have been referred to as local polar fluctuations or dynamic disorder within the literature.[37, 70] The

structure is said to be in constant motion above the tetragonal phase transition and cannot be described accurately by the harmonic picture regarding vibrational motion. This anharmonic nature has been realized within the Raman spectra of OIPs as the diffused baseline seen in the results presented with an intensity that is increasing as approaching 0 cm^{-1}. These features are also sensitive to temperature as they decrease in chloride and bromide analogs at low temperatures.[70, 71] However, this also means that with increasing temperature, it grows. Temperature-dependent ultra-low frequency Raman spectra of the single crystalline $MAPbI_3$ from Figure 12b were normalized to focus on changes regarding PbI_2 formation; however, in Figure 13a, they are presented without

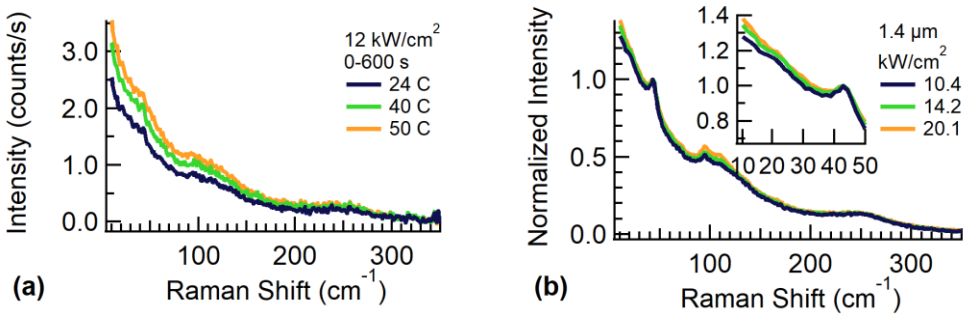

Figure 13. (a) Unnormalized spectra of single crystalline $MAPbI_3$ from Figure 12b and (b) High-power spectra for 1.4 µm film normalized at ~45 cm^{-1}.

normalization. Spectra here were collected under the same excitation power, and all changes are attributed to heat application. Below 200 cm^{-1}, the overall intensity increases as 0 cm^{-1} is approached, and a peak at ~45 cm^{-1} is observed. Also shown in Figure 13b are the high-power spectra of the 1.4 µm film. Spectra are collected at different excitation powers and signal-to-noise ratios; therefore, they have been normalized to the peak at ~45 cm^{-1} to demonstrate the subtle differences. This ~45 cm^{-1} peak has been reported for the tetragonal phase of $MAPbI_3$.[69] It is said to reduce in intensity as the lattice expands, approaching the higher temperature cubic phase of the structure. This 45 cm^{-1} peak was

present in all polycrystalline domain sizes with little difference but moderately visible within Figure 13a. The more prominent presence in the polycrystalline film may suggest some other differences between them and the single crystal. Also, below 200 cm^{-1} in the thin film (Figure 13b), the overall signal increase is slight, as shown in the inset, where the region below 50 cm^{-1} suggests heating due to the excitation power is relatively small.

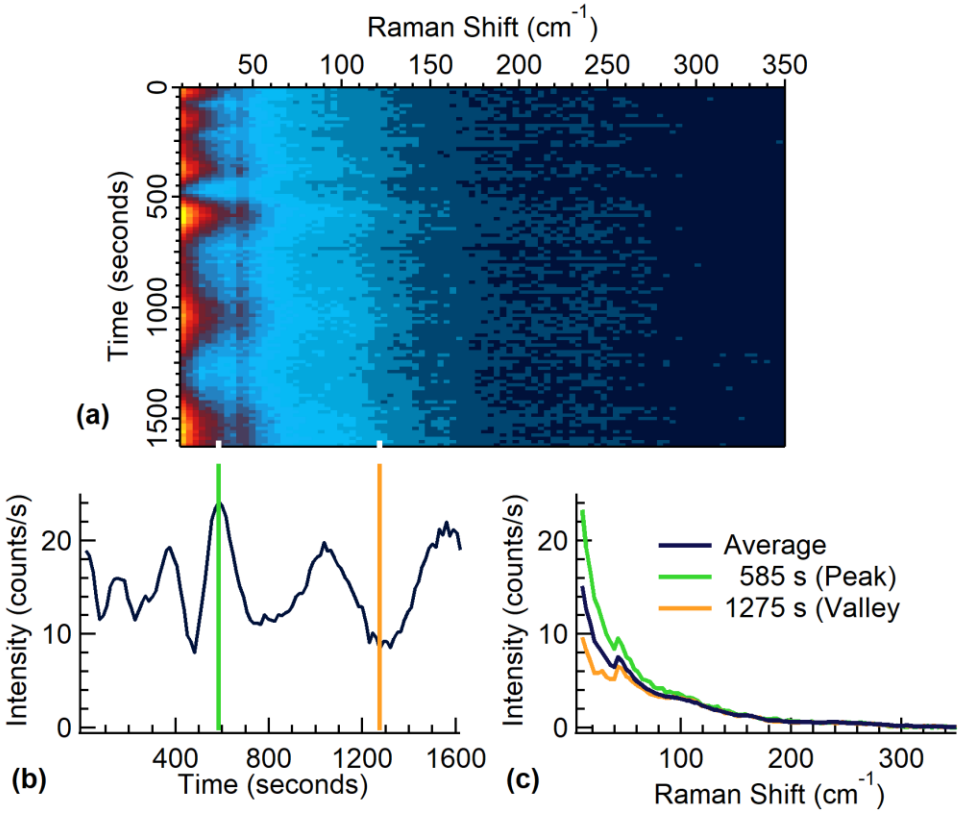

Figure 14. (a) Raman Intensity Map over time for Single Crystal. (b) Intensity below 20 cm^{-1} fluctuations over time, and (c) representative spectra.

The dynamic nature and fluctuations within $MAPbI_3$ have been reported to occur on the pico and femtosecond time scales[37, 90] and are likely too fast to be readily detected by Raman spectroscopy. However, in a few instances, large fluctuations were seen on time scales on the order of seconds. Figure 12a demonstrated normalized spectra to track the evolution over time on single crystalline $MAPbI_3$, where iodide-related species formed with broad peaks at ~110 and ~160 cm^{-1}. Figure 14 shows these results without

normalization. An intensity map (Figure 14a) of the Raman spectrum over time shows that this near 0 cm^{-1} region is the most intense (bright red and yellow) and fluctuates, also shown graphically in Figure 14b. These fluctuations can span seconds or even tens of seconds, a much longer time scale than fluctuations reported. Two periods in time are marked, one where the intensity below 20 cm^{-1} is high (green line) and another where the intensity is low (orange line), and their spectra have been plotted in Figure 14c along with the average spectrum through the total time. This region approaching 0 cm^{-1} is changing drastically relative to the rest of the spectral features. It has been suggested that the dynamic disorder in these unique structures can evolve as slow-moving displacements that also can decrease charge carrier overlap.[37] Perhaps this is an indication of such effects. Such intensity fluctuations in this region have been reported to oscillate with polarization and are dependent on the crystallographic orientation of the structure under measurement.[69, 70] The crystal orientation was not considered during measurements. It could indicate why it was seen occasionally, and further experiments will be needed to obtain a clearer picture of the dynamics.

3.6 Summary

Even though moisture can induce degradation more slowly,[38] polycrystalline films measured under ambient conditions did not form PbI_2 until an excitation power threshold was surpassed, regardless of its domain size. Below this threshold, the Raman signal at 95 cm^{-1} increased following a negative exponential function due to a more defective or disrupted structure forming at the surface. In the large single crystal, defect-related iodide species resulted in Raman peaks at ~110 and ~160 cm^{-1} from long-term illumination or higher excitation densities before PbI_2 formation. These results indicate how the synthesis

method affects the material structure and photodegradation process. Such variations in synthesis methods have already been shown to affect the trap properties in solar cell devices.[25] Udalova et al. also witnessed PbI_2 appearing readily within thin films under photoexcitation, but in the case of powder samples, iodine and polyiodide species had increased generation along with PbI_2.[88] However, thin films have also displayed these similar peaks,[44, 91] perhaps further indicating that different thin-film fabrication methods result in different spectra from additional surface contributions, grain structures, or relative concentrations of photodegradation products. One such possibility could be the precursor molar ratio used during synthesis. Son et al. showed that a methylammonium iodide (MAI) layer formed at the grain boundaries even with a 6% mole excess of MAI precursor.[92] This layer could provide the conditions for increased iodine and polyiodide-generated species in thin films. Ni et al. have also shown that interstitial iodide defects (I_i^+) are more prevalent with increasing MAI precursors during synthesis, which upon electron capture (I_i^0), can participate toward $2I_i^0 \rightarrow I_2$ and irreversible degradation.[74] Polycrystalline films in this study were synthesized by the two-step method and were unlikely to result in MAI excess conditions. For this reason, iodine-related species were not seen or are not as abundant to be detected readily.

The polycrystalline films and the single crystal formed PbI_2 only once a threshold was surpassed. In the thin films above 8 kW/cm^2, PbI_2 growth scaled linearly with excitation power as it started on the surface. At the same time, initially, iodine-related species formed under illumination in the large single crystal. At higher excitation or additional heating into the cubic phase at a lower comparable excitation induced PbI_2 formation. Both results suggest that photocarrier generation and heating can affect the

degradation process. Charge carriers have been reported to cause photostriction effects, which are proportional to illumination intensity, that expand the lattice due to the reduction of the hydrogen bonding strength of MA with the inorganic backbone structure[93] and have also been reported to reduce the activation energy of ion migration, further accelerating degradation[94], suggesting MA is mobile in the presence of charge carriers. The linear growth of PbI_2 with high-power excitation likely arises from increased charge carrier concentrations. The presented results suggest that the role of the domain size and, ultimately, the surface acts as a method of escape for MA and iodine-related species and acts as a boundary that increases the effective concentration of charges as localization and trapping can occur.[73] This is one reason why even at the comparable threshold power used for the single crystal, PbI_2 is only seen after an intentional cubic phase transition as a higher threshold occurs. MA is less tightly bound due to the reduced hydrogen bonding of this phase and is more mobile. Along with these photoinduced compositional changes, large structural fluctuations were also observed and occurred on time scales spanning tens of seconds, much longer than reported fluctuations, demonstrating the overall dynamic and easily deformable nature of the $MAPbI_3$ structure under photoexcitation.

CHAPTER 4: Carrier Transport Properties of $MAPbI_3$ Compared to GaAs

4.1 Overview

Film synthesis methods affect the morphology, like domain size[53] and the relative distribution of defect and trap states.[24, 25] These characteristics have been shown to affect the stability of $MAPbI_3$ and arise with iodine-related[23, 74] or PbI_2[38, 66, 73] products. However, concerning optical and electronic properties, defects and traps are often treated or said to be "benign":[15, 16, 95] producing shallow states with energies close to the band edge, reducing nonradiative processes and allowing for long-lived excited states and high emission yields for these unique classes of materials.

The transport properties of $MAPbI_3$, however, have varied throughout the literature,[28] much like the stability. The range of synthesis techniques and characterization methods may also contribute to these deviations. For instance, carrier diffusion in polycrystalline $MAPbI_3$ has been reported to be ~100 nm. Still, in lightly chlorine-doped films, it reached ~1 μm.[6] Chlorine-doped methods were suspected to improve crystallinity and optical properties,[44] demonstrating the role of the specific synthesis method used. These values were also determined by PL quenching measurements, where an acceptor layer was placed into contact with the thin film. This strategy is widely used for transport characterization with the diffusion equation; however, diffusion is modified in the presence of a carrier acceptor region and no longer the intrinsic value,[50, 96] possibly adding uncertainty. Values observed for single crystals are even more drastic, with one report indicating carrier diffusion reaching >175 μm, even up to 3 mm depending on the photoexcitation density.[7] The long carrier diffusion was reasoned by reduced defects in these materials and obtained by photocurrents

measured, where one type of carrier (e.g., hole) is collected near the electrode where photoexcitation occurs. To produce the observed photocurrent, the opposite type carrier (e.g., electron) must traverse the entire thickness of the material. However, such conditions do not indicate intrinsic carrier diffusion: the average distance charge carriers travel due to a concentration gradient before recombining. Under the applied bias that induces a drift current, one carrier has no opposite for extended periods to allow for recombination, increasing that carrier's lifetime.[26] Within the same study on single crystals, the carrier mobilities, which are related to the carrier diffusion using the Einstein relation, also varied depending on the technique used. Hole mobilities of 164 ± 25 and 105 ± 35 $cm^2\ V^{-1}\ s^{-1}$ were obtained for space charge limited current (SCLC) and Hall effect measurements, respectively. Such methods apply a bias and ultimately depend on the condition of the electrical contact.[28] Also, the classic SCLC method might not be valid for $MAPbI_3$.[97] Just like charge carriers, the applied bias can induce the migration of ions[25, 94] within the structure, which can lead to collapse. Electric potentials generally have this ability in hybrid perovskites, where the ions are not as firmly bound as in most conventional inorganic semiconductors. This results in significant ionic conductivity in most transport or electrical property characterization. Most notably, the J-V hysteresis reported throughout the literature is directly related to the trap and surface states due to the migration of ions and defects.[25] All these instances suggest that defects are not entirely "benign" and add to the complexity of the transport study. Additionally, as revealed within the current work by use of a PL imaging technique, photon recycling could also lead to an artificially long carrier diffusion length.

Device efficiencies for halide perovskites are comparable to typical semiconductor equivalents, often with the former's high emission efficiency and long carrier diffusion given as explanations. In the case of carrier diffusion, however, they are often compared to organic materials with inferior device performance. Instead, they should be compared to materials like GaAs, which perform much more similarly.[5, 15] $MAPbI_3$ is said to have carrier properties much like GaAs, with small effective masses and similar carrier scattering processes.[28, 52] A comparison with GaAs provides a chance to describe and contrast with a material considered the standard and said to be somewhat similar. Both materials are probed by directly measuring the charge carrier transport without a carrier quencher or electrode in an all-optical manner, eliminating the role of an applied potential or carrier drift and reducing a possible contributing source of induced ion and defect migration within the halide perovskite.

4.2 Transport Properties of $MAPbI_3$ and GaAs

Fabrication methods play a significant role in the material characteristics and, ultimately, the properties displayed. A $MAPbI_3$ thin film (UNC-U) of ~200 μm size domains displayed uniform optical properties from measurements conducted using a 50x (0.95 NA) objective lens with chromatic correction. Figure 15a shows a PL peak intensity map displaying only a 1.6% deviation under 532 nm excitation (~2.33 eV). A GaAs double-heterostructure (B2206) measured at a comparable excitation (Figure 15b) indicates only a 2.0% deviation showing how these materials are relatively uniform optically. However, a drastic difference in the relative intensities between the two films by a factor of ~40 demonstrates the high emission yields of the hybrid perovskite material. The PL spectra also show different characteristics. For the perovskite, the PL

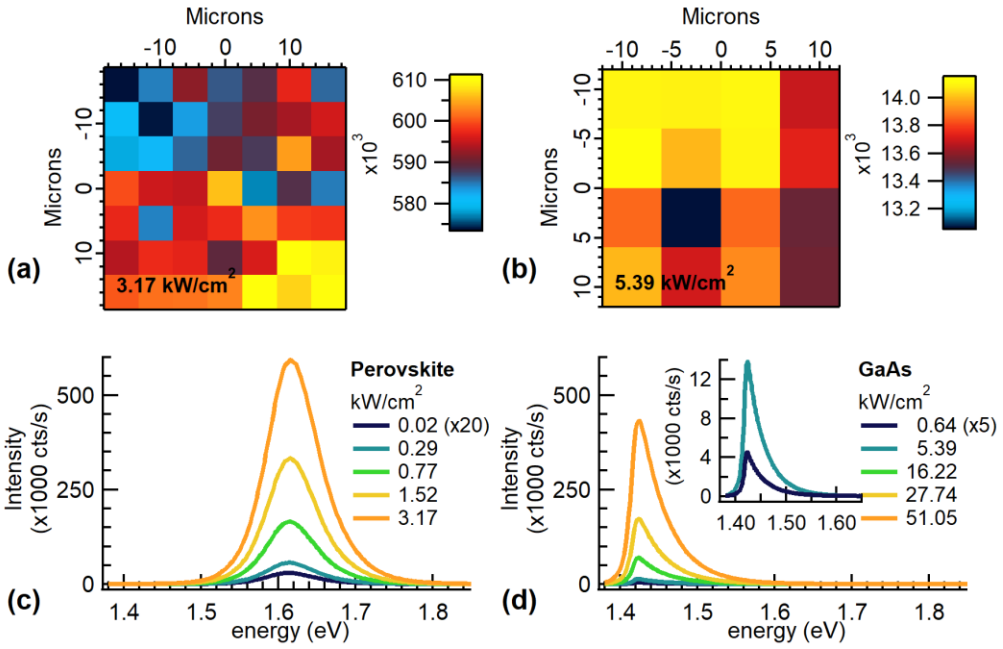

Figure 15. PL peak intensity maps for (a) $MAPbI_3$ and (b) GaAs at a comparable excitation density. PL spectra with increasing excitation for (c) $MAPbI_3$ and (d) GaAs.

peak is centered at ~1.61 eV (770 nm) with minimal change (max ~2 meV shift) under varying excitation power (Figure 15c). At the same time, GaAs reaches peak intensity at ~1.42 eV (873 nm) (Figure 15d), with a max ~2 meV shift with excitation power. Apparent is the shape difference of these spectral bands. $MAPbI_3$ is more symmetric and broader, while the GaAs double-heterostructure demonstrates a more asymmetric character with more deviations toward higher energies. Typically, the higher energy side reflects information regarding carrier thermalization and follows a Boltzmann distribution.[33] In contrast, the lower energy side experiences broadening due to electron-phonon coupling, disorder, or impurities/defects.[15] Significant broadening and the gaussian-like shape of the PL band of $MAPbI_3$ suggest that disorder and defects play an essential role in the optical properties.

Primarily, electrical methods have been used to determine the carrier transport properties,[28] which can be affected by ion migration[29] that induces changes in the local

material composition, including the doping level.[24] PL imaging is an all-optical method used to alleviate this issue where excitation is focused onto the material where photons emitted by photogenerated carriers that have diffused away from the excitation site are captured by an optical camera. For thin films, the 2D diffusion profile is described by a modified Bessel function (7), from which the diffusion length is obtained by least-squares fitting.[15, 51]

$$I = C * K_0(\frac{r}{L_d}) \tag{7}$$

K_0 is a modified Bessel function of the second kind, L_d the diffusion length, C a normalization constant, and r the radius from the excitation site. Figures 16a and 16b

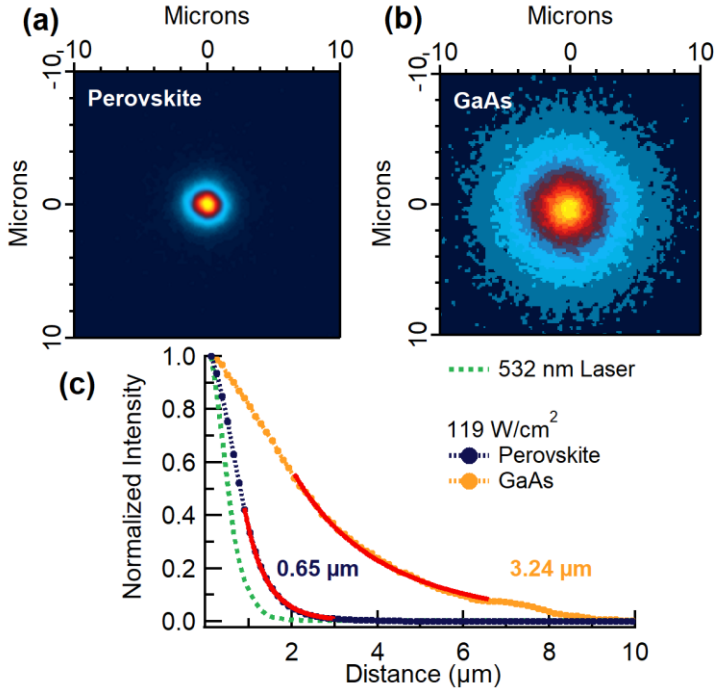

Figure 16. PL Images of (a) $MAPbI_3$ and (b) GaAs under 119 W/cm^2 excitation along with (c) average diffusion profiles and calculated diffusion lengths.

show PL images of photons emitted near the respective PL peak energy for the perovskite and GaAs film, where considerable intensity arises away from the excitation site at (0,0).

These images were collected under 119 W/cm^2 photoexcitation and demonstrate that carriers are more localized or closer to the excitation site in the perovskite film than in GaAs. In taking an angular average about the excitation site, an average emission profile can be obtained and is displayed in Figure 16c, along with fits to (7) and calculated diffusion lengths within these films. This $MAPbI_3$ film demonstrated vastly superior relative emission yields (Figure 15) but has a modest diffusion length of 0.65 μm at this excitation density. At the same time, the GaAs film shows a carrier diffusion length ~5 times larger at 3.24 μm even though emission intensities under these excitation conditions were ~400 times smaller at the excitation site. Although the more considerable carrier diffusion in GaAs reduces the emission at the excitation site, the effect only accounts for a small fraction of the difference in the collected emission intensity. These results suggest that the lower energy broadening observed within the $MAPbI_3$ PL spectrum and, therefore, the nature of the structure may play a significant role in restricting carrier diffusion. Even within GaAs, restricted carrier diffusion is known to occur upon introducing structural disorder, reducing losses at defects.[98]

4.3 Effects of Trap States on Charge Carrier Diffusion

Defect states accumulate charge carriers and can induce losses through nonradiative processes, thus, reducing emission yields. Monitoring the PL intensity as excitation density increases can provide insight into the various recombination pathways within a material.[99] Defect states will trap carriers lowering efficiency due to nonradiative recombination, but as carrier generation increases (increased photoexcitation), they appear no longer a hindrance once traps have become filled. This often results in increased PL efficiency and ultimately means that carrier transport properties are a

function of the carrier density present. Different regimes from competing processes such as Shockley–Read–Hall (SRH) or bimolecular radiative recombination can be empirically described by the relationship in (8)[100]

$$I_{em} = C * {I_{ex}}^{b} \tag{8}$$

where I_{em} and I_{ex} are the emission and excitation intensities, C is a normalization constant, and the power law coefficient b reflects the recombination processes present. Under only bimolecular radiative recombination, the power law coefficient b approaches

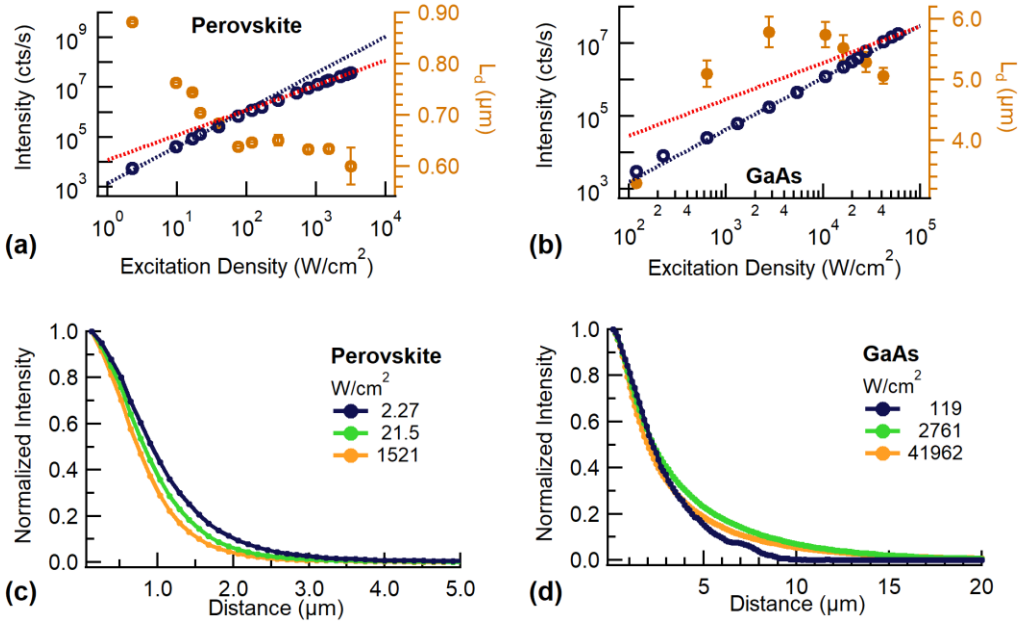

Figure 17. Integrated PL with excitation density for (a) $MAPbI_3$ and (b) GaAs. Average emission profiles for (c) $MAPbI_3$ and (d) GaAs from low to high excitation.

1, but above, a more complex I_{ex} function often arises as nonradiative effects such as SRH are also present.[101] Figures 17a and 17b show the changes within the integrated intensity as photoexcitation increases (dark blue circles) for both materials collected with a (0.95 NA) 50x objective lens with chromatic correction and a spot size of 1032 nm. Two dashed lines are also plotted, each indicating a different regime. The black dashed lines fit (8) where SRH contributes with b values of 1.47 and 1.43 for $MAPbI_3$ and GaAs,

respectively. The red dashed lines indicate when traps have become filled and bimolecular radiative recombination is dominant (b = 1). Both materials undergo SRH as expected at lower excitation densities as defect and trap states are primarily vacant. However, $MAPbI_3$ then undergoes a transition to bimolecular recombination at higher excitation suggesting traps become filled, while GaAs may appear to approach this regime at even higher excitation densities. Also displayed in Figures 17a and 17b are select fitted diffusion lengths (L_d, brown-filled circles) with typical errors for select excitation powers. Carrier diffusion typically increases upon filling defects and traps,[96] of which can be seen within GaAs (Figure 17b). The diffusion length begins at 3.2 µm, rising to a maximum of 5.9 µm throughout the range where trap recombination is present (SRH, black dashed lined). After this peak, it decreases, possibly resulting from an increase in the radiative recombination rate (proportional to the carrier density),[101] reducing the carrier lifetime. Average emission profiles in Figure 17d for GaAs show that carrier travel distances increase from low (dark blue) to increasing excitation (green). However, at higher densities, it begins to decrease (orange). This carrier diffusion relative to the laser spot (1032 nm) could also reduce the integrated intensity as carriers can travel outside the confocal volume.[101] In the perovskite film, the diffusion length does not increase within the measured excitation range. Instead, it drops from an initial value of 0.88 µm, approaching a constant value of ~0.64 µm (Figure 17a). An increased deviation at the highest excitation density may have resulted from structural changes. Figure 17c demonstrates the decreasing carrier travel in the average profiles as excitation increases. This result is interesting as the regime where trap recombination contributes is seen (black dashed line) and, therefore, should be realized with an increasing diffusion length

within this range as traps fill. Still, their presence does not affect the carrier diffusion similarly to a typical inorganic semiconductor like GaAs.

What is restricting carrier diffusion even upon filling trap states and reducing possible nonradiative recombination in the perovskite? The diffusion length (L_d) depends on both the diffusivity (D) and the carrier lifetime (τ) as $L_d = \sqrt{D\tau}$ (equation 2). D is sensitive to temperature but less so to doping levels and the concentration of defects. However, τ is sensitive to doping levels and the concentration of defects. The carrier lifetime often exhibits a maximum between two extremes. One when nonradiative recombination is dominant in the low excitation region and the other in the high excitation region where radiative recombination is dominant.[101] This excitation density dependence is shown in Figure 17b for GaAs. Compared to GaAs, one possibility is that the measured excitation range for $MAPbI_3$ does not contain the lower extreme where nonradiative recombination is dominant. Though relatively lower excitation densities were measured on $MAPbI_3$, the material has a significantly higher radiative recombination rate.[15] The diffusion length may be restricted by carrier scattering due to the structural disorder within the perovskite, and the carrier lifetime is either longer or comparable to the scattering time. Upon increasing excitation density, it is further reduced by an increasing radiative recombination rate, as shown in GaAs, leading to a shortening of the carrier diffusion length.

Raman spectroscopy measurements could not be incorporated on these specific films as the experimental conditions differ among the Raman and PL imaging methods. For instance, for $MAPbI_3$, PL images are captured within 1 sec and can easily reach saturation of the optical camera under increasing excitation densities and exposure times.

At the same time, the Raman signal is weak, especially under photoexcitation, needing longer integration times. The Raman signal was also time-dependent, making it challenging to replicate the same conditions. However, it should be mentioned that the probed excitation range (Figure 17a) for $MAPbI_3$ coincides with the low-power regime observed earlier in Chapter 3 (Figure 6b), where the surface becomes progressively more distorted or defective before reaching the stability threshold and structural collapse. Though different methods were used to synthesize the polycrystalline films, defect formation has been reported to help dissipate excess energy within this excitation range from the slowed carrier cooling in $MAPbI_3$, resulting in a distorted structure and changes in optical properties.[102] In $MAPbI_3$ nanocrystals, modified optical properties also occurred as photogenerated carriers were trapped within the "benign" shallow states but could still contribute toward signal from defect-stimulated emission.[95] However, upon surface passivation, the optical properties were improved due to the reduced trapping of these photogenerated carriers. These reports suggest that the surface or defects could also play a role in the observed carrier localization with increased excitation densities for $MAPbI_3$. For both $MAPbI_3$[103] and $MAPbBr_3$,[104] large radiative recombination centers occur on the surface.

4.4 Morphology and Surface Effects on Charge Carrier Diffusion

The surface and morphology may play a role in the carrier transport properties of $MAPbI_3$. An oxysalt surface passivated[57] film formed by blade coating (UNC-B)[58] was probed to understand these effects better. Blading coating has gathered traction for large-scale processing, viewed as more efficient than spin-coating.[20] Optical images in Figure 18a display that this film is nonuniform. Macro domains of ~50 μm are present, further

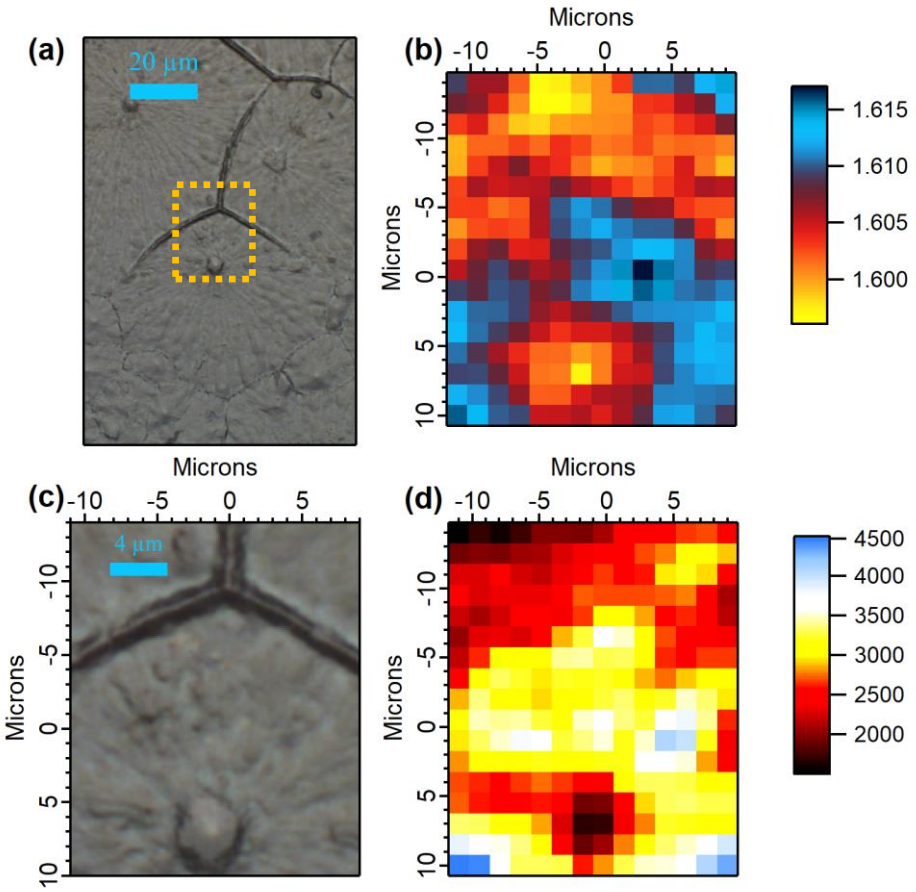

Figure 18. (a) Optical image of $MAPbI_3$ blade-coated film. (b) PL peak energy and (d) PL peak intensity maps of the (c) corresponding region with a polygon domain.

composed of surface features down to ~250 nm in size. Apparent and readily seen within these optical images are more prominent features ~3-5 μm in size, referred to as polygon domains, with one shown at the bottom in Figure 18c. Within this optical image is seen how the surface is not uniform, with some regions appearing thicker than others. This nonuniformity is also present within this film's emission properties, shown in Figures 18b and 18d. Figure 18b displays the PL peak energy where some regions are relatively redshifted, most notably the polygon domain. Such redshifts have been suggested to arise from differences in thickness and agree with this more prominent feature.[100] In the

regions with higher energy (blue areas) in Figure 18b, relatively higher emission intensities (yellow and white spots) are observed (Figure 18d).

In contrast, the redshifted or lower energy (red) areas have lower emission intensities, with the most obvious case being the polygon domain showing the darkest regions (dark red and black). These maps were collected in a raster scan fashion without any changes in focus as each pixel was measured, indicating that differences in relative depth could arise with regions being measured close to the surface and others farther away within the bulk. Possible reasons for the decreased intensity in the suspected thicker areas could be that excited carriers diffuse out of the confocal collection volume[15] or possible reabsorption of photons[100] before escaping from the material.

Three areas on this blade-coated film are compared with the uniform film (UNC-U) measured in Sections 4.2 and 4.3. Both films were formed by blade-coating, except for alkylamines added within the precursor solution used to create the uniform film. This again illustrates how the specific synthesis method affects the film properties. PL spectra of a redshifted (Red) and blueshifted (Blue) location along with the polygon domain are compared with the spectrum from the uniform film in Figure 19a. The intensities at these locations vary, along with the PL peak energy. The uniform film (UNC-U) resembles the spectrum corresponding to the blueshifted (Blue) location on the nonuniform material (UNC-B), at least energetically, with peak energies similar at 1.614 and 1.613 eV, respectively. Peak energies decrease to 1.604 and 1.592 eV in the redshifted (Red) region and the polygon domain. In measuring the changes in integrated PL intensity with excitation density (Figure 19b), the Blue and Red locations resemble the uniform film (UNC-U) at higher densities. However, these regions on the nonuniform material (UNC-

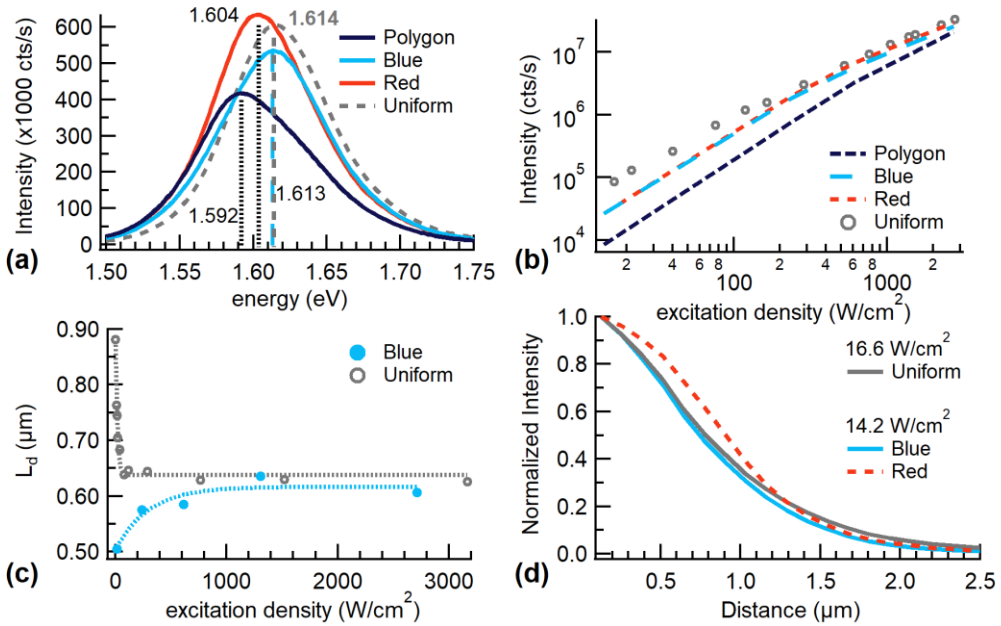

Figure 19. Comparing (a) PL spectra and changes in (b) emission intensities on blade-coated films. (c) Increasing carrier diffusion and (d) shape differences in diffusion profiles.

B) displayed reduced emission intensities at lower excitation. This can indicate increased SRH recombination within the more nonuniform blade-coated film (UNC-B) from a more extensive distribution of defects and traps. Changes in diffusion length (Figure 19c) for the Blue location suggest this is the case where an increase occurs before it becomes an almost constant value similar to that seen within the uniform film (dashed lines for ease of visualization). An initial rise occurred within the GaAs double-heterostructure (Figure 17b), which had also undergone passivation of its surfaces. However, it was not observed in the uniform perovskite film (Figures 17a and 19c). It could further suggest that the more uniform film (UNC-U), with its reduced defect distribution implied by higher emission intensities at lower excitation (Figure 19b), undergoes a decreasing diffusion length from an increasing radiative recombination rate with excitation. The average emission profiles display similarities between the blueshifted location (Blue) and

the uniform film (Figure 19d) at a comparable excitation density. However, comparing the redshifted and possibly thicker region (Red) showed a significant change in the profile at distances closer to the excitation site. It also gave inadequate fits to (7), suggesting that more processes may occur besides 2D diffusion.

Changes within the diffusion profile are even more drastic within the polygon domain (Figure 20). An optical image of the polygon domain and its corresponding PL image are shown in Figures 20a and 20b. Immediately apparent, the relative intensity of

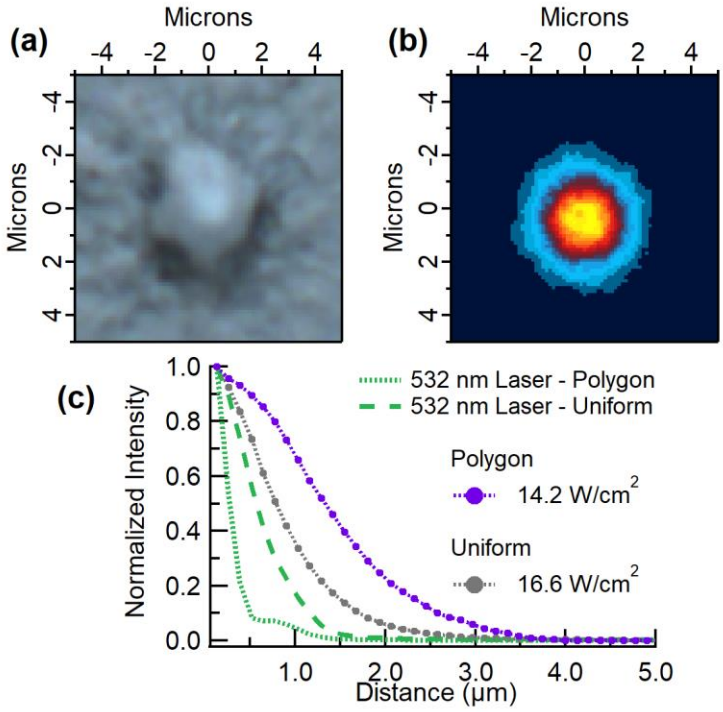

Figure 20. (a) Optical and (b) PL images of polygon domain and (c) comparing emission and laser profiles with the uniform film.

emission seems to coincide with the approximate physical dimensions of this feature (~4.5 x 4.5 μm), suggesting that physical boundaries confine carriers. This drastic relative increase in emission away from the excitation site is further demonstrated within the emission profiles (Figure 20c). The profile for the uniform film has been displayed at a comparable excitation density (grey), and it becomes evident that a more significant

portion of carrier emission reaches farther distances within the polygon domain (purple). Photoexcitation was likely occurring within the polygon domain away from the surface since focus readjustments for this feature were not done. The emission collected could be out of focus from the excitation volume resulting in a broadening of the profile. However, the laser excitation collected under identical conditions to Figure 20b, which likely experiences a distortion of the shape from excitation within the material, is not drastically broader or out of focus compared to the laser profile on the uniform film (Figure 20c), which was focused to the surface of the film, suggesting other processes are indeed occurring. Like the profile from the redshifted region (Red) in Figure 19d, the emission profile for the polygon domain could not be modeled by (7) and suggest that excitation in thicker areas, perhaps within the bulk and away from the surface, extends carrier diffusion or introduces other effects. A dependence on thickness has also been seen within $MAPbBr_3$ single crystals, where carrier lifetimes and mobilities differed within different portions of the crystal and away from the surface.[105]

4.5 Photon Recycling and Thicker Materials

From the previous section, measured diffusion lengths in $MAPbI_3$ films were on the order of a micron (Figure 19c). Energetic shifts also occurred within the PL spectra, possibly correlated with differences in thickness, and resulted in extended or modified carrier spatial profiles that could not be modeled by 2D diffusion. Extended transport properties within halide perovskites are often explained by long carrier diffusion or other processes like photon recycling. During photon recycling, photons are reabsorbed instead of emitted or scattered out of the material after they were initially generated. Suppose the internal quantum efficiency of radiative recombination is sufficiently high, and there is

considerable overlap between the emission and absorption spectrum. In that case, several cycles of photon recycling can proceed, resulting in emission distances farther than the initial excitation site.[106] In work by Pazos-Outón et al., photons collected at the edge of their $MAPbI_3$ film progressively redshifted as photoexcitation occurred further from the collection site.[107] Photon recycling was suggested because tens of micron distances arose between the photoexcitation site and the redshifted photons collected. Photon recycling is a primary contributor to why GaAs solar cell devices maintain the current single-junction device efficiency record.[108] However, photons collected at the edge originate from weak

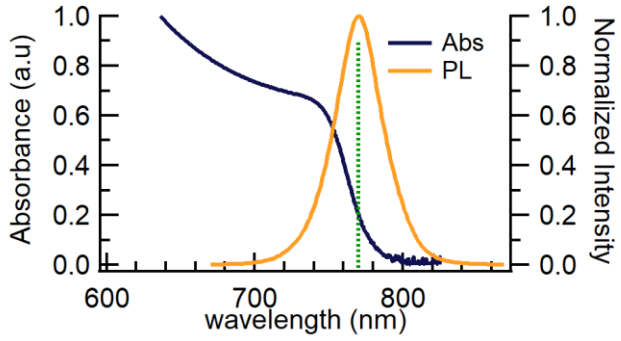

Figure 21. Absorption and PL spectrum of uniform $MAPbI_3$.

absorbing band edge states and cannot effectively contribute to the recycling process. Instead, they are laterally guided optical waves that result in losses.

There is an interplay of several kinds of photons within $MAPbI_3$ upon photoexcitation. Photons emitted at or near the excitation site (carriers diffused away) and those that have traveled within the material. In the last case, these photons are trapped within the film due to the narrow escape cone or the waveguide effect that arises from the high refractive index ($n\sim2.6$) of $MAPbI_3$.[109] They can travel via total internal reflections, scattering out, or be reabsorbed and remitted. Reabsorption requires the material's traveling internal photon and absorption profile to overlap and is likely to occur

with higher energies above the bandgap. Figure 21 demonstrates the decreased absorption of energies below the PL peak (dashed vertical line) for the uniform $MAPbI_3$ film (UNC-U). The absorption depth also decreases as higher energies are readily absorbed, resulting in changes more likely to occur within shorter distances. All this could lead to the photon recycling process (reabsorption and reemission) only happening near the excitation site and possibly the modifications observed in the carrier emission profiles in the thicker or redshifted regions within the nonuniform blade-coated film (UNC-B). The redshifted spectra arose from a decreased contribution of higher energies due to reabsorption. This interplay among the various photon contributions within the obtained spectra depends on the surface, collection method, morphology, and thickness.[110] Surface passivation and other layers can also affect this dynamic, meaning the displayed optical properties of the material within a device can be different from the free film. This makes the overall method of simple PL observation somewhat difficult to quantify within a nonuniform material, just like that shown within the nonuniform blade-coated $MAPbI_3$ film.

4.6 Energy-Dependent Photon Contributions in $MAPbI_3$ and GaAs

Pazos-Outón et al. used two objective lenses in their work evaluating photon recycling: one was stationary at the edge of their film in collection mode.[107] At the same time, the other was moved incrementally farther from the edge providing the photoexcitation source. Our PL imaging system can measure and capture where photoluminescence is emitted or escaping from the material. Two objectives are unnecessary and not preferred. As in our system, the entire spatial field can be probed by capturing the spatial distributions of photons with specific energies selected by bandpass filters. Photons near the PL peak and those with lower energies demonstrate similar

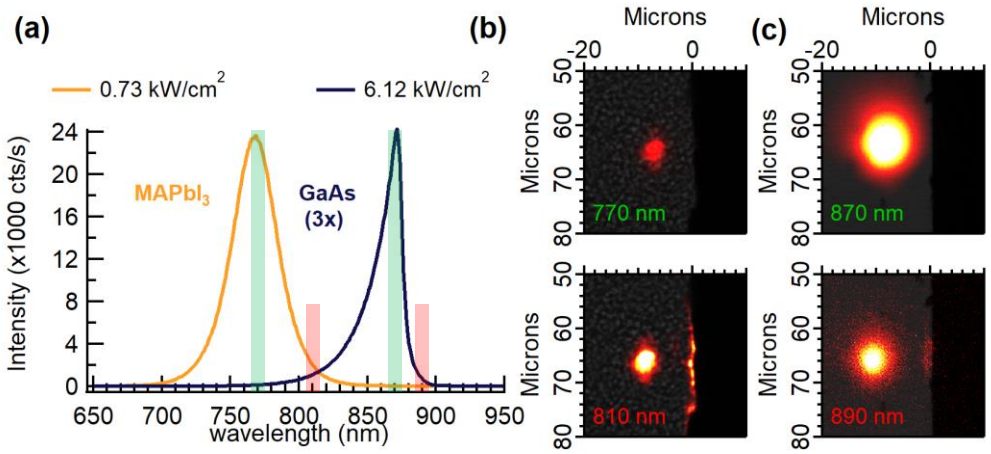

Figure 22. (a) Peak (green) and lower energy (red) distributions probed for $MAPbI_3$ and GaAs. Composite images for (b) $MAPbI_3$ and (c) GaAs.

results to those by Pazos-Outón et al., where emission at the edge of the material arises from lower energy photons in both the double-heterostructure GaAs (B2206) and a PMMA passivated $MAPbI_3$ film (TOL). Figure 22a displays the photon distributions measured at both materials' PL peak (green) and below the peak (red). At the same time, Figures 22b and 22c show composite images where the PL image has been overlaid on the optical image to illustrate that when photons at the PL peak are selectively observed, they are only seen near the excitation site. When photons are seen near the excitation site and the physical edges, they are from only lower energies. GaAs, with its lower PL efficiency and reduced contribution of these lower energies, produced a weak signal with increased noise, as shown in the bottom image of Figure 22c (890 nm).

Photoexcitation over 30 microns from the edge still indicated these lower energy photons escaping, traveling some distance much longer than the carrier diffusion. This edge emission is suggested to contribute a large portion of all externally emitted photons in $MAPbI_3$ at ~50%.[110] In the $MAPbI_3$ film, however, the various photon distributions probed show differing effects on the emission profile obtained. The high energy (blue),

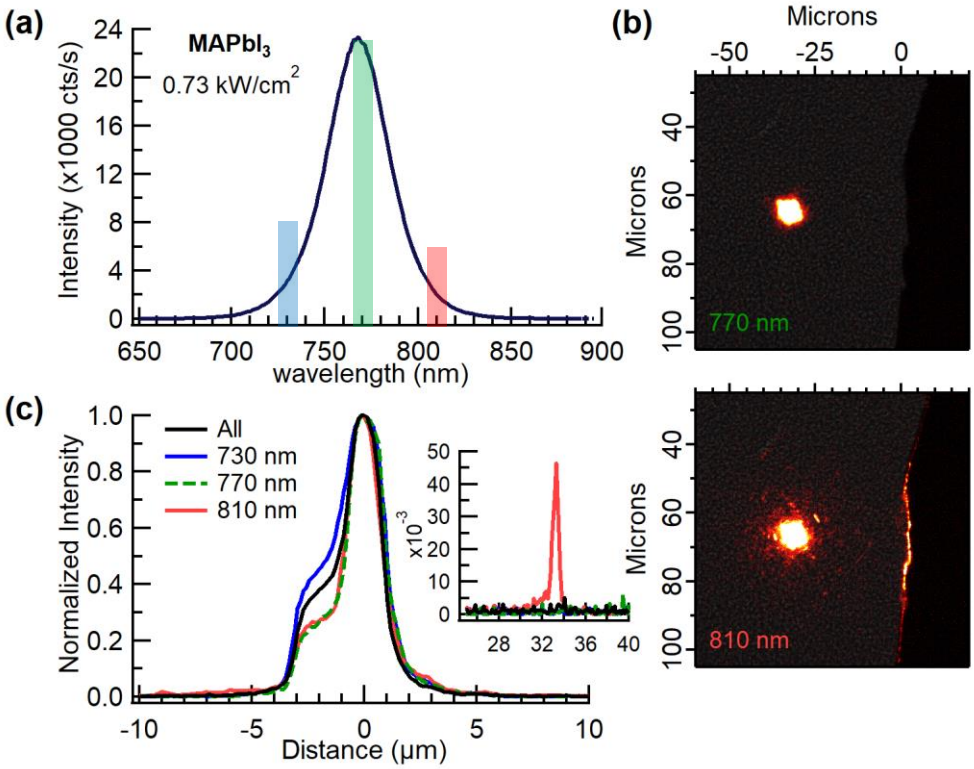

Figure 23. (a) High (blue), Peak (green), and lower (red) energy distributions probed. (b) Composite images for Peak and low energies and (c) horizontal line profiles across the excitation site. (inset: emission escaping at edge ~33 μm)

PL peak (green), and low energy distributions (red) considered are shown in Figure 23a. In the PL peak and lower energy PL images (Figure 23b), lower energy photons (810 nm) are even observed escaping at other locations from the top surface before reaching the edge. This likely arises because the film is polycrystalline with significant surface roughness. It has been reported that a more defective and distorted surface could induce blueshifts in the PL spectrum,[40] resulting in a shift in the absorption gap and reducing the reabsorption of lower energies.[102] Therefore, surfaces can act as scattering centers for these energies.[110]

Additionally, spatially anisotropic carrier diffusion or propagation of emitted light has been observed. This dynamic of photons reabsorbed and scattered is further

demonstrated when considering higher energies. Spatial emission profiles are asymmetric in these $MAPbI_3$ films (TOL); however, this asymmetry can be used to observe how the nearby regions reabsorb and remit higher energies. It is difficult to monitor changes from high-energy images as they appear like the images at the PL peak energy. However, emission profiles from horizontal line scans across the excitation site (at distance = 0) towards the edge (distance > 0) readily show differences in Figure 23c. At the PL peak (770 nm) and lower energies (810 nm), the profiles are similar by the excitation site. The central emission intensity peak arises along with a shoulder on the left (distance < 0), indicating inhomogeneity in the film structure. However, at the edge (inset) ~33 μm away, an intensity peak is seen only from lower energy 810 nm photons that have escaped. With higher energies (730 nm), the relative contribution of the shoulder (nearby region) increases compared to the longer wavelength components. In the case of all photon energies collected, the relative contribution of the shoulder is within the two extremes. This is unexpected because, in a uniform system, the higher energy carriers are expected to have the same diffusion length as those at lower energies in a near-equilibrium state or a slightly shorter diffusion length due to relaxation to the lower energy states. A possible explanation could be that the polycrystalline domain to the left has higher crystallinity and, thus, is more able to reabsorb photons and remit from the surface (photon-recycling). In contrast, the longer wavelength emission is more likely to propagate laterally due to the waveguide effect.

4.7 The Role of defects in GaAs

Due to its microscopic nature, a dislocation type defect is challenging to visualize in the GaAs double-heterostructure (B2206) from the surface. However, their presence

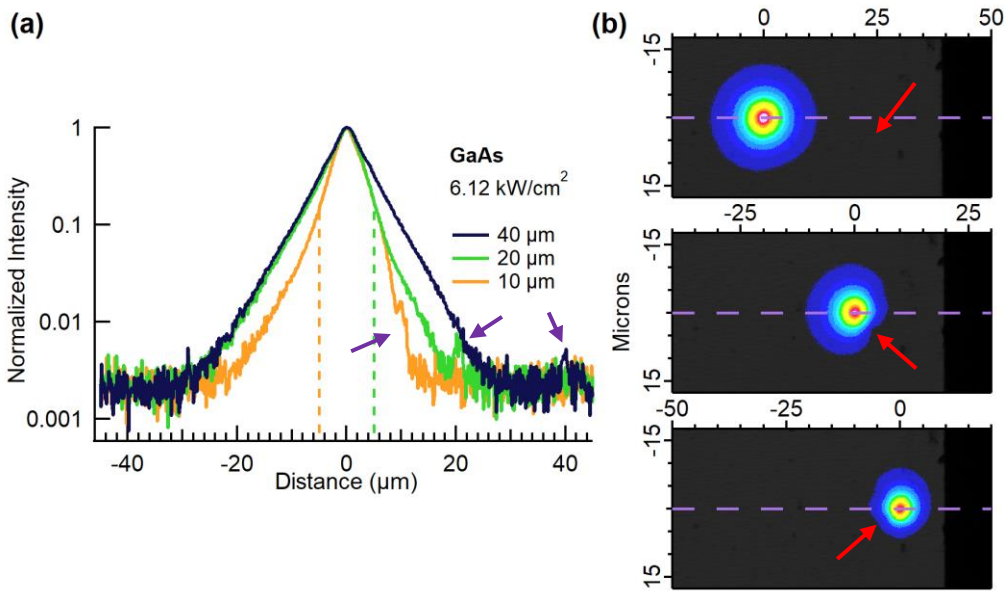

Figure 24. (a) Emission profiles from all energies approaching the edge (indicated by purple arrows) and a defective region indicated by vertical dashed lines corresponding with the same color. (b) Composite images at various distances from the edge. Red arrows indicate the positions of the interior defect.

can be observed by their effects on the carrier recombination and diffusion properties. There are multiple ways to probe the defect with PL-based techniques, for instance, confocal PL scan[96] and PL imaging under widefield illumination.[50] This work illustrates another way: wide-field PL imaging using a focused beam for excitation. This approach can more directly reveal how the defect, serving as a quencher, affects the carrier diffusion. In GaAs, a dislocation-like defect was found at ~15 μm from one edge. Figure 24a show emission profiles (from all photon energies) at different excitation sites along a horizontal line, nearly passing the defect perpendicular to the edge. Emission intensities across the excitation site are modified while approaching the edge in the presence of the defect. When the excitation is at ~40 μm from the edge, the emission profile is weakly affected by the defective area, showing a near-symmetric profile. Photons also escape at the edge (purple arrow). These photons at the edge are relatively weak and not easily

visible within the PL image (top of Figure 24b) but readily seen in the line scan profile (~40 μm). At ~20 μm from the edge, the profile is changed drastically, showing faster decay towards the edge (positive distance) by the defective area (green vertical dashed line) but unchanged away from the edge, almost identical to the profile at ~40 μm. This asymmetry is also apparent within the PL image (middle of Figure 24b), as the defective location (red arrow) can attract carriers. At ~10 μm, reduced intensity occurs on both sides of the excitation site where away from the edge, the defective region (orange dashed vertical line) affects the emission profile, and towards the edge, possibly a combination of the same defective region and the physical boundary of the material itself as shown in Figure 24a and the bottom of Figure 24b (red arrow). The results demonstrate how an acceptor (quencher) region can distort the transport characteristics, yielding a reduced diffusion length. Since nonradiative processes are more prevalent in GaAs than $MAPbI_3$, carriers are more readily lost in these defective locations.[15]

4.8 Single Crystalline $MAPbI_3$

Polycrystalline $MAPbI_3$ films suggest that distorted or defective regions like the surface affect how photons of specific energies are reabsorbed or scattered throughout the material (Figure 23). Single crystalline $MAPbI_3$ offers a material with reduced surfaces and grain boundaries to observe more clearly what occurs without their presence. Figure 25a shows a visually flat portion of a much larger (millimeters) cleaved $MAPbI_3$ single crystal (TOL-S). When all emitted energies are collected, intensity is readily seen continuing towards the right edge of the region. At the same time, photons are also detected at the edges towards the bottom of the area (red arrow). By monitoring specific energies, several trends become apparent.

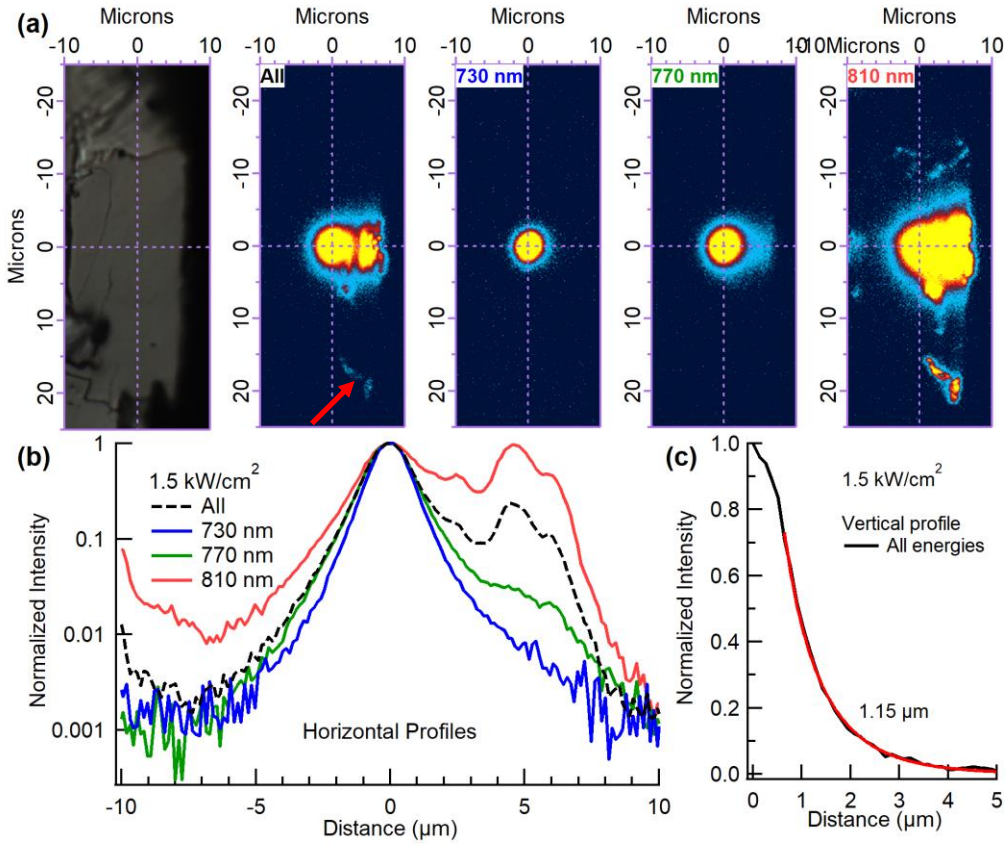

Figure 25. (a) Optical and PL images at various energies for single crystalline $MAPbI_3$. (b) Emission profiles from the PL images across the horizontal 0 line. (c) Vertical emission profile and calculated diffusion length.

Intensity is detected much closer to the excitation site when only higher energies are measured (730nm). When energies are reduced, near 770 nm (PL peak), the intensity region extends overall with noticeable increases towards the right of the area. This intensity region broadens even more drastically at the lowest energies (near 810 nm). This increase appears to be continuous from the excitation site before becoming more sporadic, like the polycrystalline film (bottom of Figure 23b), when the edge is approached. Photon reabsorption effects have already been suggested to occur in single continuous crystals, unlike polycrystalline materials, where other dynamics have been proposed to explain the PL shifts, like Rashba splitting.[110]

Horizontal line profiles across the region's center (Figure 25b) show the changes graphically within the PL images. With higher energies (blue), emission intensity is reduced overall as the distance from the excitation site increases compared to the PL peak energies at 770 nm (green). The trend in the polycrystalline film (Figure 23c) was reversed where the PL peak energies had reduced intensities near the excitation site in the nearby region. The increase in relative intensities at farther distances for this single crystal is most pronounced at the lowest energies (810 nm), comparable to the excitation site. Across the vertical profile (Figure 25c), emission intensity is more symmetric with a determined diffusion length of 1.15 μm. This continuous change and increase in relative intensity in the horizontal direction from higher to lower energies indicate how more easily higher energies are reabsorbed as intensities decrease rapidly from the excitation site. It is unclear why the asymmetry in the two directions occurs, but the reduced concentration of distorted surfaces and abrupt breaks within the crystal indicate that other effects are happening. Figure 23c showed that when higher energies were only monitored in the presence of more surfaces within the polycrystalline film, the intensities of the nearby region were increased. This possibly could be explained by the distorted surfaces absorbing higher energies and emitting a higher energy photon. In the continuous crystal, reabsorption could likely result in a lower energy photon being reemitted. However, several additional peaks and photons detected sporadically suggest that scattering centers still occur within this single crystal from possible nonuniformity.

4.9 Detectable Photocurrent in $MAPbI_3$

Photocurrent studies have suggested that diffusion lengths are long in $MAPbI_3$. Over 100 microns in single crystals[7] to approaching ~10 microns or larger within

nanomaterials.[111, 112] With photocurrent detection, the rationale is that charges travel a distance comparable to the material's physical dimensions and that the process is indeed carrier diffusion.[26] However, as mentioned earlier, one carrier is typically collected first, and the remaining carrier often has a reduced amount of recombination partners to relax to the ground state, extending that carrier's lifetime and allowing it to travel considerable distances toward the counter electrode under the action of a drift field. However, this is not intrinsic carrier diffusion. The previous sections showed that photons could travel internally within the material toward the edge tens of microns away. At the same time,

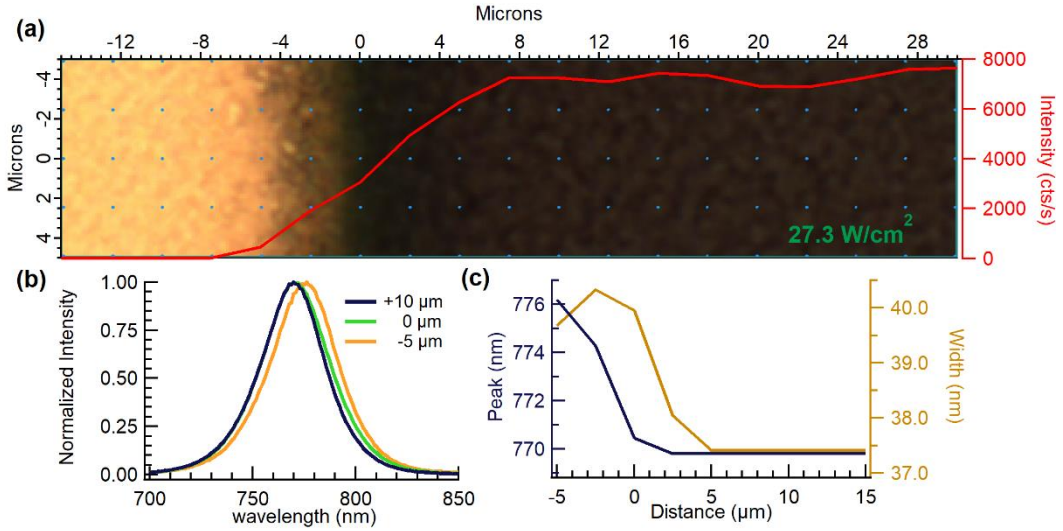

Figure 26. (a) Gold/Perovskite interface with overlaid average PL intensity (red). (b) Spectral changes with distance from the interface. (c) PL peak shifts (dark blue) and changes in spectral width (brown).

collection near the excitation site suggests that actual carrier diffusion is relatively restricted.

A PMMA passivated $MAPbI_3$ film with deposited gold electrodes (TOL-G) was measured to understand what occurs to the carrier population under a bias such as in the photocurrent experiment. The effects of the gold electrode on the nearby region were first evaluated optically. Figure 26a shows the interface where the gold electrode and the

perovskite meet at a distance labeled ~0 μm. The grid points show locations where the PL spectrum was collected with the average intensity indicated by the red curve. Far from the electrode, the average intensity approaches ~8000 cts/s but decreases below ~8 μm from the interface. The spectrum not only experiences a peak intensity reduction but an increase in width towards lower energies and, eventually, a redshift of the entire band (Figure 26b). These effects also occur at differing distances in the vicinity of the electrode (Figure 26c). The width (brown) increase begins within 5 μm from the interface. At the same time, the overall peak redshift (dark blue) begins within ~2.5 μm from the interface and continuously redshifts into the gold layer. The gold/$MAPbI_3$ interface is said to undergo band bending from the Schottky contact formed.[113] These effects could arise with an electric field that can readily separate charges, possibly reducing the nearby emission intensity, and affecting the higher energy carriers more, which might explain the red shift and broadening. Another explanation could be that the region experienced compositional changes during the electrode deposition, such as becoming more defective.

Emission profiles from horizontal line scans collected near the gold electrode also show interesting effects. Figure 27a demonstrates emission profiles collected when excited at ~5 μm from the interface (set as the origin). When monitoring only the intensity at the PL peak energy, the profile does not appear to be affected by the nearby gold (dark blue). However, when considering only the lower energies, a peak appears (gold), like the peak that arises from photons escaping at the edge of the material. The PL image of these lower energies (Figure 27b) shows that this smaller peak occurs at the gold/perovskite interface, indicating that lower energy photons can reach the electrode

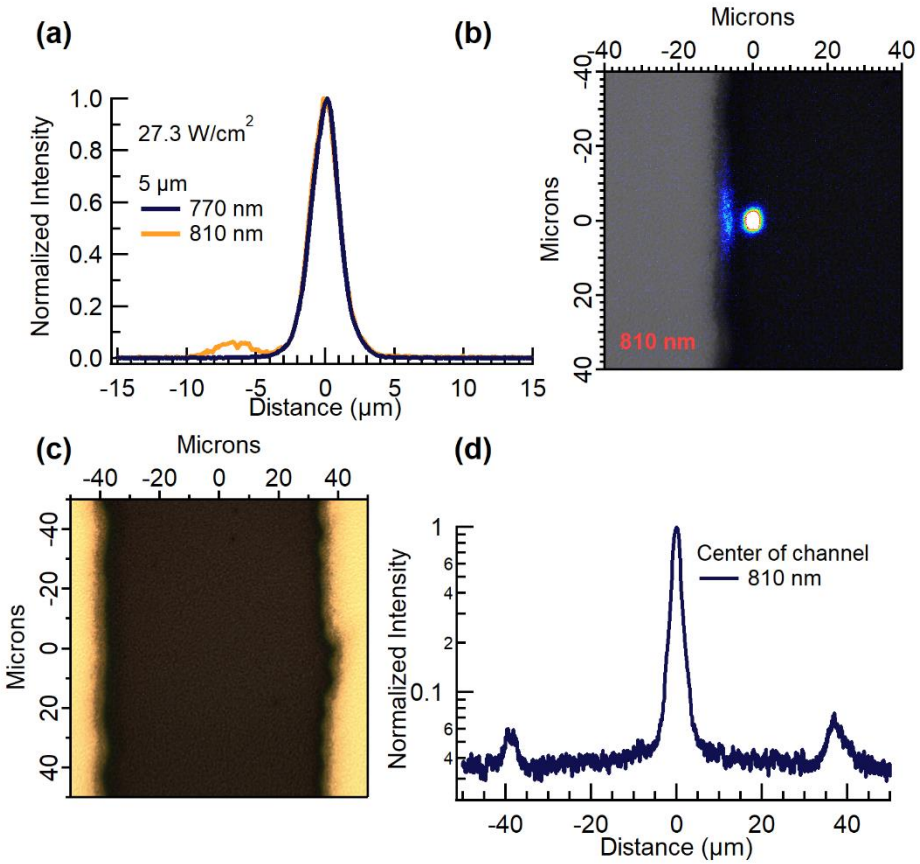

Figure 27. (a) Emission profiles 5 µm from the gold/perovskite interface. (b) Low energy composite image near the gold electrode. (c) Optical image of 70 µm electrode channel and (d) low energy emission profile from excitation in the center.

even though the carriers are limited and localized near the excitation site. This is further demonstrated by photoexcitation within a ~75 µm channel formed by two gold electrodes (Figure 27c). In monitoring the lower energy emission profile (Figure 27d) from photoexcitation in the center of this channel, two additional peaks are again observed at the two gold/perovskite interfaces demonstrating how far these photons can travel.

Under an applied electrical field, ion migration occurs, resulting in hysteresis. The field that causes ions to migrate can also apply force on the excited carriers, changing pure carrier diffusion to coexisting carrier diffusion and drift. In the similar $MAPbBr_3$ structure, nanoplates with ~20 µm gold electrode channels demonstrated carrier drift

increasing with an applied bias up to 5V within their imaging measurements.[114] Such conditions could allude to the interpretation of "long" carrier diffusion within these materials as carrier drift.

The PMMA passivated $MAPbI_3$ film (TOL-G) had gold electrodes deposited with several channel widths. A smaller ~30 µm gold channel was probed under a bias to observe whether carrier drift readily occurs in these polycrystalline films as less voltage would be required to induce comparable effects to those seen within the mentioned

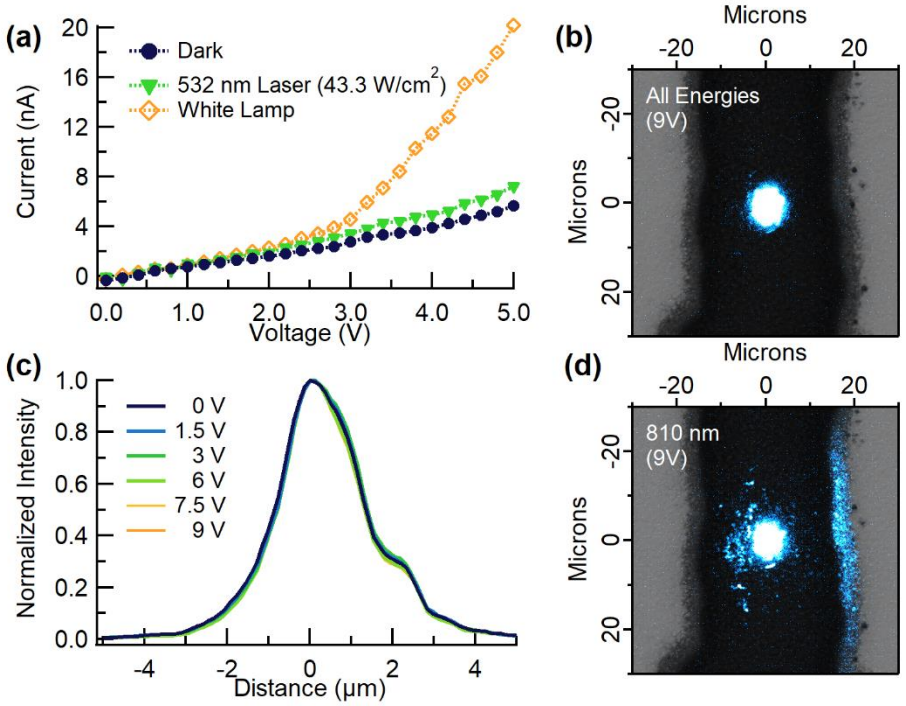

Figure 28. (a) Photocurrent from laser and white light illumination. Composite images within 30 µm channel for (b) all energies and only (d) low energies (810 nm). (c) Emission profiles from all emission energies under different applied biases.

$MAPbBr_3$ nanoplates.[114] Current-Voltage measurements indicated a photoresponse above the dark current (dark blue) in Figure 28a. Focused 532 nm excitation (0.36 µW, 43.3 W/cm^2) at the center (green) of the channel shows an increase in current, with the effects even more pronounced under larger area white lamp illumination (gold). However, PL

imaging showed that emission intensity is localized near the excitation site (Figure 28b), even under 9 V or ~3 kV/cm, with the positive electrode on the left side.

Carrier diffusion remains short within these materials, even upon evaluating the emission profile of all emitted energies under various applied potentials (Figure 28c). These horizontal intensity profiles do not deviate largely, suggesting that the drift effect does not significantly affect carrier diffusion under these conditions. However, at lower energies, it is seen that emission again can reach the electrodes and emerge from certain sites of the film surface (Figure 28d). These energies are not easily seen within Figure 28b (all energies) because the higher energy contributions are more prevalent. These results suggest that the initial carrier distribution at the excitation site is still restricted, but the lower energy traveling photons can readily approach the electrodes.

Regarding the small photocurrent shown in Figure 28a, there are two possible mechanisms. One is that a small number of the photogenerated carriers at the center of the channel could still be collected at the electrodes through the drift mechanism. The other possibility could be that the lower energy traveling photons were reabsorbed near the electrode to generate the current. The quantum efficiency (QE) of the photocurrent generated can be estimated to be on the order of ~1.3% (photocurrent electrons/532 nm photons) after subtracting the dark current and correcting for surface reflection losses[15] to the 0.36 μW excitation density at the 5 V bias, as shown in Figure 28a. When the carrier mean free path (L_{drift}) is much smaller than the distance between the excitation site and the electrode, which is likely the case here, it is related to QE according to the Mott-Gurney photoconductivity model for single-site excitation by (9)[115]

$$QE \approx \frac{L_{drift}}{L} \tag{9}$$

where L is the channel width. Furthermore, L_{drift} can be described by (10)

$$L_{drift} = \mu E \tau \quad (10)$$

E is the electrical field, μ the carrier mobility, and τ the lifetime. With values L = 30 μm, V = 5 V, and QE ≈ 1.3%, a μτ product is approximately 2.3 10^{-8} cm^2/V. If mobility ranges on the order of 1 cm^2 V^{-1} s^{-1} are assumed, for solution-processed $MAPbI_3$ films determined in electrodeless methods,[28] then a value of τ ~ 23 ns is obtained. However, the electrode region possibly also has the necessary conditions for reabsorption of the traveling photons and charge separation, as a Schottky contact is said to occur at the gold/perovskite interface. As shown earlier (Figure 26), this interface demonstrates an increased width and optical redshift, possibly providing the conditions for increased reabsorption of these lower energies and producing a photocurrent. A quantitative estimate of this process is less straightforward. Still, the internal PL quantum efficiency could be close to 100% under the excitation density used,[15] and the reabsorption of a small fraction of the emitted photons near the electrode could potentially yield the level of the current observed. Additional measurements would be needed to distinguish between the two possibilities. Therefore, explaining the photocurrent generated by long-distance carrier diffusion is inappropriate, with either being possible.

4.10 Summary

"Benign" defects are thought to arise in $MAPbI_3$ with states near the band edges. These states do not largely contribute to nonradiative processes. However, carrier diffusion decreases with photoexcitation in uniform blade-coated films even upon filling trap states. Unlike a GaAs double-heterostructure, where the filling of traps results in an initial increase in the carrier diffusion. With increasing excitation densities and relatively

lower defect concentrations, more significant carrier concentrations may increase the radiative recombination rate, thus, lowering the carrier lifetime and diffusion length. As shown earlier, the $MAPbI_3$ structure within this excitation range could become more distorted by defect formation (Chapter 3). However, it is difficult to know if this is indeed contributing.

Photoexcitation away from the surface in thicker regions within an oxysalt-passivated blade-coated film (UNC-B) also demonstrated that different processes likely occur away from surfaces, such as the increased probability of photon reabsorption. This additional process manifested within the measured emission profiles as increased intensities closer to the excitation site, likely from an increased likelihood of higher energy photon reabsorption and a redshift of the obtained PL spectrum. In contrast, lower energy photons can travel far within films due to a decreased reabsorption probability and the narrow escape cone that arises from the high refractive index of the material. These traveling internal photons were observed in both $MAPbI_3$ and GaAs using PL imaging, where edge emission occurred only when lower energies were selectively observed. These travel distances appeared to be quite large, reaching tens of microns. In the polycrystalline $MAPbI_3$ film, these lower energy photons also scattered out at other locations before going to the edge. Possibly due to the polycrystalline nature of the material, with more defective surfaces or domain boundaries present. Distortions in the perovskite structure shift the absorption gap to higher energies making lower energy reabsorption less probable. The reverse was also observed when nearby domains had increased emission contributions with higher energies within the PL imaging measurement. While in GaAs, defects are much more challenging to observe.[116]

However, they can be detected by monitoring the spatial variation in emission intensity. The defective regions, which could not be seen on the surface, distorted carrier diffusion several microns away, showing how an acceptor region with increased nonradiative processes modifies the transport properties. In $MAPbI_3$ single crystals with the reduction of surfaces and defects, the reabsorption probability of emitted photons was increased. This arose within PL images and emission profiles with a continuous decrease in intensity at distances farther from the excitation site at higher energies.

The carrier diffusion appears restricted due to the perovskite structure, especially within the polycrystalline films. However, photocurrent measurements within the literature have suggested that carrier diffusion lengths can reach 10s of microns,[111, 112] even over a hundred microns in single crystals.[7] However, films deposited with gold electrodes showed that lower energy photons could reach the gold/perovskite interface even upon photoexcitation within the center of a ~75 μm gold electrode channel. While still, the initial carrier distribution formed by the excitation site was restricted. Even upon application of a bias within a ~30 μm gold electrode channel, emission profiles indicated no significant deviations from the pure diffusion dictated profile as emission was still localized near the excitation site at the center of the channel. Yet, these materials registered a photocurrent under the same laser excitation density. This could be explained by the drift effect or the traveling lower energy internal photons still reaching the electrode/perovskite interface. This region, from PL measurements, indicated that the area is modified possibly by the potential Schottky contact formed, which can separate charges from the increased probability of reabsorption of the lower energy traveling photons and produce a current.

CHAPTER 5: Conclusions and Future Work

5.1 Conclusions

The organic-inorganic hybrid perovskite displays remarkable optical properties that rival and even surpass typical inorganic semiconductors under some circumstances. Low deep-level trap concentrations and efficient radiative recombination have demonstrated that $MAPbI_3$ can compete with semiconductors such as GaAs in the low excitation density region.[15] However, while optical properties are impressive, the material is susceptible to various environmental factors of instability, including moisture,[38] heating,[64] and even photoexcitation.[23] It was shown that photoexcitation causes a surface disturbance, eventually leading to decomposition and PbI_2 formation. With increasing surfaces, decomposition occurs more readily, leading to a higher fraction of degraded material. This was seen in measuring the domain size dependence on the photodegradation process using Raman spectroscopy. Not only did a higher PbI_2 content form in smaller domains with an increased surface area, but it also occurred faster. Demonstrating that more attention is needed regarding the film's physical properties during characterization. Within the literature, film characteristics are often not reported or, if rarely so, deviate from one study to another, often leading to failure to form a consensus on general properties such as the Raman spectrum.[39] Different synthesis methods are often used. Here, it is suspected that even with precursor molar ratios, differences can arise with varying contributions of photodecomposition products, as observed in the iodide-related species formed from single crystals but not in polycrystalline materials measured.

The film properties also affect the carrier transport observed within $MAPbI_3$. Carrier transport properties were determined using an all-optical photoluminescence imaging technique. This method removed the possible errors typically found in electrical methods, such as induced ion migration or carrier drift. The carrier diffusion length observed in polycrystalline films ranges from ~0.6 - 0.9 μm depending on the photoexcitation density. Despite the higher relative emission efficiencies of $MAPbI_3$ compared to an inorganic semiconductor like GaAs, the latter displayed a much larger diffusion length. The disordered nature of $MAPbI_3$ broadens the photoluminescence spectrum and restricts carrier transport. In nonuniform films of varying thickness, carrier emission intensities observed using the PL imaging method deviated from 2D carrier diffusion when excitation occurred within the bulk and away from the surface, leading to a modification of the PL emission profiles at close distances to the excitation site. Surfaces and defective areas can induce blue shifts in the photoluminescence spectrum[40] and the absorption energy threshold, allowing reabsorption only likely to occur from higher energies. The obtained diffusion lengths appear small compared to reports using photocurrent methods.[111, 112] This discrepancy was probed by conducting the photocurrent measurement on $MAPbI_3$ films with gold electrodes in combination with PL imaging demonstrating that carrier diffusion is still limited within polycrystalline films even under an applied electrical field. One possible explanation for measured photocurrents is from traveling internal low-energy photons that can reach a possible Schottky junction at the perovskite/gold interface, where reabsorption of the traveling low-energy photons produces a photocurrent. Another possibility could be carrier drift under the applied electric field.

5.2 Future Work

The $MAPbI_3$ structure is deformable, and its ions are in constant motion. Large structural fluctuations occurred at lower wavenumber frequencies on the order of seconds, much longer than typically reported,[37] under photoexcitation on several occasions. Within the literature, such oscillations at these frequencies modulate with excitation polarization;[69, 70] however, observing it over time could indicate a change in polarization within the structure. Further work would require materials with known crystal orientations to further probe these oscillations, which may not have been reported prior under continuous photoexcitation.

Carrier transport properties were measured on polycrystalline films as well as single crystals. Polycrystalline materials with gold electrodes under a bias demonstrated minimal carrier drift. However, perovskite nanoplates have shown that carrier drift can be imaged under a bias within the literature.[114] Perhaps, this is also a by-product of the increased grain boundaries and surfaces within the polycrystalline film, further restricting carrier transport. To clarify this discrepancy, thin single crystalline or nanomaterials such as nanoplates with gold electrodes should be probed. In the mentioned nanoplates, carrier drift followed the photogenerated minority carrier and was shown to change or reverse under bias.

Furthermore, $MAPbI_3$ was the model system used in this work. It is the most known, however unstable, compared to mixed perovskite analogs, which are more directly applicable to constructed devices.[20] With long-term stability being the main limiting factor towards commercialization and photoexcitation itself being a source of instability, these hybrid versions should be further evaluated under similar methods.

References

(1) Shen, Q.; Ogomi, Y.; Chang, J.; Toyoda, T.; Fujiwara, K.; Yoshino, K.; Sato, K.; Yamazaki, K.; Akimoto, M.; Kuga, Y.; et al. Optical absorption, charge separation and recombination dynamics in Sn/Pb cocktail perovskite solar cells and their relationships to photovoltaic performances. *J. Mater. Chem. A* **2015**, *3* (17), 9308-9316, DOI: 10.1039/c5ta01246e

(2) Xing, G.; Mathews, N.; Lim, S. S.; Yantara, N.; Liu, X.; Sabba, D.; Gratzel, M.; Mhaisalkar, S.; Sum, T. C. Low-temperature solution-processed wavelength-tunable perovskites for lasing. *Nat. Mater.* **2014**, *13* (5), 476-480, DOI: 10.1038/nmat3911

(3) Tan, Z. K.; Moghaddam, R. S.; Lai, M. L.; Docampo, P.; Higler, R.; Deschler, F.; Price, M.; Sadhanala, A.; Pazos, L. M.; Credgington, D.; et al. Bright light-emitting diodes based on organometal halide perovskite. *Nat. Nanotechnol.* **2014**, *9* (9), 687-692, DOI: 10.1038/nnano.2014.149

(4) Noh, J. H.; Im, S. H.; Heo, J. H.; Mandal, T. N.; Seok, S. I. Chemical management for colorful, efficient, and stable inorganic-organic hybrid nanostructured solar cells. *Nano Lett.* **2013**, *13* (4), 1764-1769, DOI: 10.1021/nl400349b

(5) Green, M. A.; Hishikawa, Y.; Dunlop, E. D.; Levi, D. H.; Hohl-Ebinger, J.; Yoshita, M.; Ho-Baillie, A. W. Y. Solar cell efficiency tables (Version 53). *Prog. Photovoltaics Res. Appl.* **2019**, *27* (1), 3-12, DOI: 10.1002/pip.3102

(6) Stranks, S. D.; Eperon, G. E.; Grancini, G.; Menelaou, C.; Alcocer, M. J.; Leijtens, T.; Herz, L. M.; Petrozza, A.; Snaith, H. J. Electron-hole diffusion lengths exceeding 1 micrometer in an organometal trihalide perovskite absorber. *Science* **2013**, *342* (6156), 341-344, DOI: 10.1126/science.1243982

(7) Dong, Q.; Fang, Y.; Shao, Y.; Mulligan, P.; Qiu, J.; Cao, L.; Huang, J. Solar cells. Electron-hole diffusion lengths > 175 mum in solution-grown CH3NH3PbI3 single crystals. *Science* **2015**, *347* (6225), 967-970, DOI: 10.1126/science.aaa5760

(8) Kieslich, G.; Sun, S.; Cheetham, A. K. Solid-state principles applied to organic–inorganic perovskites: new tricks for an old dog. *Chem Sci* **2014**, *5* (12), 4712-4715, DOI: 10.1039/c4sc02211d

(9) Walsh, A. Principles of Chemical Bonding and Band Gap Engineering in Hybrid Organic-Inorganic Halide Perovskites. *J. Phys. Chem. C* **2015**, *119* (11), 5755-5760, DOI: 10.1021/jp512420b

(10) Weller, M. T.; Weber, O. J.; Henry, P. F.; Di Pumpo, A. M.; Hansen, T. C. Complete structure and cation orientation in the perovskite photovoltaic methylammonium lead iodide between 100 and 352 K. *Chem. Commun.* **2015**, *51* (20), 4180-4183, DOI: 10.1039/c4cc09944c

(11) Bakulin, A. A.; Selig, O.; Bakker, H. J.; Rezus, Y. L.; Muller, C.; Glaser, T.; Lovrincic, R.; Sun, Z.; Chen, Z.; Walsh, A.; et al. Real-Time Observation of Organic Cation Reorientation in Methylammonium Lead Iodide Perovskites. *J. Phys. Chem. Lett.* **2015**, *6* (18), 3663-3669, DOI: 10.1021/acs.jpclett.5b01555

(12) Poglitsch, A.; Weber, D. Dynamic disorder in methylammoniumtrihalogenoplumbates (II) observed by millimeter-wave spectroscopy. *J. Chem. Phys.* **1987**, *87* (11), 6373-6378, DOI: 10.1063/1.453467

(13) Walsh, A.; Scanlon, D. O.; Chen, S.; Gong, X. G.; Wei, S. H. Self-regulation mechanism for charged point defects in hybrid halide perovskites. *Angew. Chem. Int. Ed.* **2015**, *54* (6), 1791-1794, DOI: 10.1002/anie.201409740

(14) Yin, W.-J.; Shi, T.; Yan, Y. Superior Photovoltaic Properties of Lead Halide Perovskites: Insights from First-Principles Theory. *J. Phys. Chem. C* **2015**, *119* (10), 5253-5264, DOI: 10.1021/jp512077m

(15) Zhang, F.; Castaneda, J. F.; Chen, S.; Wu, W.; DiNezza, M. J.; Lassise, M.; Nie, W.; Mohite, A.; Liu, Y.; Liu, S.; et al. Comparative studies of optoelectrical properties of prominent PV materials: Halide perovskite, CdTe, and GaAs. *Mater. Today* **2020**, *36*, 18-29, DOI: 10.1016/j.mattod.2020.01.001

(16) Steirer, K. X.; Schulz, P.; Teeter, G.; Stevanovic, V.; Yang, M.; Zhu, K.; Berry, J. J. Defect Tolerance in Methylammonium Lead Triiodide Perovskite. *ACS Energy Lett.* **2016**, *1* (2), 360-366, DOI: 10.1021/acsenergylett.6b00196

(17) Ho-Baillie, A. W. Y.; Sullivan, H. G. J.; Bannerman, T. A.; Talathi, H. P.; Bing, J.; Tang, S.; Xu, A.; Bhattacharyya, D.; Cairns, I. H.; McKenzie, D. R. Deployment Opportunities for Space Photovoltaics and the Prospects for Perovskite Solar Cells. *Adv. Mater. Technol* **2021**, *7* (3), 2101059, DOI: 10.1002/admt.202101059

(18) Nagabhushana, G. P.; Shivaramaiah, R.; Navrotsky, A. Direct calorimetric verification of thermodynamic instability of lead halide hybrid perovskites. *PNAS* **2016**, *113* (28), 7717-7721, DOI: 10.1073/pnas.1607850113

(19) Zhang, Y.-Y.; Chen, S.; Xu, P.; Xiang, H.; Gong, X.-G.; Walsh, A.; Wei, S.-H. Intrinsic Instability of the Hybrid Halide Perovskite Semiconductor CH3NH3PbI3*. *Chin. Phys. Lett.* **2018**, *35* (3), 036104, DOI: 10.1088/0256-307x/35/3/036104

(20) Jena, A. K.; Kulkarni, A.; Miyasaka, T. Halide Perovskite Photovoltaics: Background, Status, and Future Prospects. *Chem. Rev.* **2019**, *119* (5), 3036-3103, DOI: 10.1021/acs.chemrev.8b00539

(21) Wang, D.; Wright, M.; Elumalai, N. K.; Uddin, A. Stability of perovskite solar cells. *Sol. Energy Mater. Sol. Cells* **2016**, *147*, 255-275, DOI: 10.1016/j.solmat.2015.12.025

(22) Yu, X.; Qin, Y.; Peng, Q. Probe Decomposition of Methylammonium Lead Iodide Perovskite in N2 and O2 by in Situ Infrared Spectroscopy. *J. Phys. Chem. A* **2017**, *121* (6), 1169-1174, DOI: 10.1021/acs.jpca.6b12170

(23) Motti, S. G.; Meggiolaro, D.; Barker, A. J.; Mosconi, E.; Perini, C. A. R.; Ball, J. M.; Gandini, M.; Kim, M.; De Angelis, F.; Petrozza, A. Controlling competing photochemical reactions stabilizes perovskite solar cells. *Nat. Photonics* **2019**, *13* (8), 532-539, DOI: 10.1038/s41566-019-0435-1

(24) Wang, Q.; Shao, Y.; Xie, H.; Lyu, L.; Liu, X.; Gao, Y.; Huang, J. Qualifying composition dependent p and n self-doping in CH3NH3PbI3. *Appl. Phys. Lett.* **2014**, *105* (16), 163508, DOI: 10.1063/1.4899051

(25) Sherkar, T. S.; Momblona, C.; Gil-Escrig, L.; Avila, J.; Sessolo, M.; Bolink, H. J.; Koster, L. J. A. Recombination in Perovskite Solar Cells: Significance of Grain Boundaries, Interface Traps, and Defect Ions. *ACS Energy Lett.* **2017**, *2* (5), 1214-1222, DOI: 10.1021/acsenergylett.7b00236

(26) Hodes, G.; Kamat, P. V. Understanding the Implication of Carrier Diffusion Length in Photovoltaic Cells. *J. Phys. Chem. Lett.* **2015**, *6* (20), 4090-4092, DOI: 10.1021/acs.jpclett.5b02052

(27) Wolford, D. J.; Gilliland, G. D.; Kuech, T. F.; Bradley, J. A.; Hjalmarson, H. P. Optically determined minority-carrier transport in GaAs/AlxGa1-xAs heterostructures. *Phys. Rev. B: Condens.* **1993**, *47* (23), 15601-15608, DOI: 10.1103/physrevb.47.15601

(28) Herz, L. M. Charge-Carrier Mobilities in Metal Halide Perovskites: Fundamental Mechanisms and Limits. *Acs Energy Lett* **2017**, *2* (7), 1539-1548, DOI: 10.1021/acsenergylett.7b00276

(29) Xiao, Z.; Yuan, Y.; Shao, Y.; Wang, Q.; Dong, Q.; Bi, C.; Sharma, P.; Gruverman, A.; Huang, J. Giant switchable photovoltaic effect in organometal trihalide perovskite devices. *Nat. Mater.* **2015**, *14* (2), 193-198, DOI: 10.1038/nmat4150

(30) Chin, X. Y.; Cortecchia, D.; Yin, J.; Bruno, A.; Soci, C. Lead iodide perovskite light-emitting field-effect transistor. *Nat. Commun.* **2015**, *6*, 7383, DOI: 10.1038/ncomms8383

(31) Stillman, G. E.; Wolfe, C. M.; Dimmock, J. O. Hall coefficient factor for polar mode scattering in n-type GaAs. *J. Phys. Chem. Solids* **1970**, *31* (6), 1199-1204, DOI: 10.1016/0022-3697(70)90122-8

(32) Wright, A. D.; Verdi, C.; Milot, R. L.; Eperon, G. E.; Perez-Osorio, M. A.; Snaith, H. J.; Giustino, F.; Johnston, M. B.; Herz, L. M. Electron-phonon coupling in hybrid lead halide perovskites. *Nat. Commun.* **2016**, *7* (1), 11755, DOI: 10.1038/ncomms11755

(33) Yu, P. Y. C., M. *Fundamentals of Semiconductors*; Springer-Verlag Berlin Heidelberg, 2010.

(34) Zhu, X. Y.; Podzorov, V. Charge Carriers in Hybrid Organic-Inorganic Lead Halide Perovskites Might Be Protected as Large Polarons. *J. Phys. Chem. Lett.* **2015**, *6* (23), 4758-4761, DOI: 10.1021/acs.jpclett.5b02462

(35) Park, M.; Neukirch, A. J.; Reyes-Lillo, S. E.; Lai, M.; Ellis, S. R.; Dietze, D.; Neaton, J. B.; Yang, P.; Tretiak, S.; Mathies, R. A. Excited-state vibrational dynamics

toward the polaron in methylammonium lead iodide perovskite. *Nat. Commun.* **2018**, *9* (1), 2525, DOI: 10.1038/s41467-018-04946-7

(36) Miyata, K.; Meggiolaro, D.; Trinh, M. T.; Joshi, P. P.; Mosconi, E.; Jones, S. C.; De Angelis, F.; Zhu, X. Y. Large polarons in lead halide perovskites. *Sci. Adv.* **2017**, *3* (8), e1701217, DOI: 10.1126/sciadv.1701217

(37) Schilcher, M. J.; Robinson, P. J.; Abramovitch, D. J.; Tan, L. Z.; Rappe, A. M.; Reichman, D. R.; Egger, D. A. The Significance of Polarons and Dynamic Disorder in Halide Perovskites. *ACS Energy Lett.* **2021**, *6* (6), 2162-2173, DOI: 10.1021/acsenergylett.1c00506

(38) Wang, Q.; Chen, B.; Liu, Y.; Deng, Y.; Bai, Y.; Dong, Q.; Huang, J. Scaling behavior of moisture-induced grain degradation in polycrystalline hybrid perovskite thin films. *Energy Environ. Sci.* **2017**, *10* (2), 516-522, DOI: 10.1039/c6ee02941h

(39) Pistor, P.; Ruiz, A.; Cabot, A.; Izquierdo-Roca, V. Advanced Raman Spectroscopy of Methylammonium Lead Iodide: Development of a Non-destructive Characterisation Methodology. *Sci. Rep.* **2016**, *6*, 35973, DOI: 10.1038/srep35973

(40) Grancini, G.; D'Innocenzo, V.; Dohner, E. R.; Martino, N.; Srimath Kandada, A. R.; Mosconi, E.; De Angelis, F.; Karunadasa, H. I.; Hoke, E. T.; Petrozza, A. CH3NH3PbI3 perovskite single crystals: surface photophysics and their interaction with the environment. *Chem Sci* **2015**, *6* (12), 7305-7310, DOI: 10.1039/c5sc02542g

(41) Brivio, F.; Frost, J. M.; Skelton, J. M.; Jackson, A. J.; Weber, O. J.; Weller, M. T.; Goñi, A. R.; Leguy, A. M. A.; Barnes, P. R. F.; Walsh, A. Lattice dynamics and vibrational spectra of the orthorhombic, tetragonal, and cubic phases of

methylammonium lead iodide. *Phys. Rev. B* **2015**, *92* (14), DOI: 10.1103/PhysRevB.92.144308

(42) Quarti, C.; Grancini, G.; Mosconi, E.; Bruno, P.; Ball, J. M.; Lee, M. M.; Snaith, H. J.; Petrozza, A.; Angelis, F. D. The Raman Spectrum of the CH3NH3PbI3 Hybrid Perovskite: Interplay of Theory and Experiment. *J. Phys. Chem. Lett.* **2014**, *5* (2), 279-284, DOI: 10.1021/jz402589q

(43) Nakada, K.; Matsumoto, Y.; Shimoi, Y.; Yamada, K.; Furukawa, Y. Temperature-Dependent Evolution of Raman Spectra of Methylammonium Lead Halide Perovskites, CH(3)NH(3)PbX(3) (X = I, Br). *Molecules* **2019**, *24* (3), 626, DOI: 10.3390/molecules24030626

(44) Grancini, G.; Marras, S.; Prato, M.; Giannini, C.; Quarti, C.; De Angelis, F.; De Bastiani, M.; Eperon, G. E.; Snaith, H. J.; Manna, L.; et al. The Impact of the Crystallization Processes on the Structural and Optical Properties of Hybrid Perovskite Films for Photovoltaics. *J. Phys. Chem. Lett.* **2014**, *5* (21), 3836-3842, DOI: 10.1021/jz501877h

(45) Ledinsky, M.; Loper, P.; Niesen, B.; Holovsky, J.; Moon, S. J.; Yum, J. H.; De Wolf, S.; Fejfar, A.; Ballif, C. Raman Spectroscopy of Organic-Inorganic Halide Perovskites. *J. Phys. Chem. Lett.* **2015**, *6* (3), 401-406, DOI: 10.1021/jz5026323

(46) Park, B. W.; Jain, S. M.; Zhang, X.; Hagfeldt, A.; Boschloo, G.; Edvinsson, T. Resonance Raman and excitation energy dependent charge transfer mechanism in halide-substituted hybrid perovskite solar cells. *ACS Nano* **2015**, *9* (2), 2088-2101, DOI: 10.1021/nn507345e

(47) Chen, Q.; Liu, H.; Kim, H.-S.; Liu, Y.; Yang, M.; Yue, N.; Ren, G.; Zhu, K.; Liu, S.; Park, N.-G.; et al. Multiple-Stage Structure Transformation of Organic-Inorganic Hybrid PerovskiteCH3NH3PbI3. *Phys. Rev. X* **2016**, *6* (3), 031042, DOI: 10.1103/PhysRevX.6.031042

(48) Yuan, Y.; Huang, J. Ion Migration in Organometal Trihalide Perovskite and Its Impact on Photovoltaic Efficiency and Stability. *Acc. Chem. Res.* **2016**, *49* (2), 286-293, DOI: 10.1021/acs.accounts.5b00420

(49) Snaith, H. J.; Abate, A.; Ball, J. M.; Eperon, G. E.; Leijtens, T.; Noel, N. K.; Stranks, S. D.; Wang, J. T.; Wojciechowski, K.; Zhang, W. Anomalous Hysteresis in Perovskite Solar Cells. *J. Phys. Chem. Lett.* **2014**, *5* (9), 1511-1515, DOI: 10.1021/jz500113x

(50) Chen, F.; Zhang, Y.; Gfroerer, T. H.; Finger, A. N.; Wanlass, M. W. Spatial resolution versus data acquisition efficiency in mapping an inhomogeneous system with species diffusion. *Sci. Rep.* **2015**, *5*, 10542, DOI: 10.1038/srep10542

(51) Haegel, N. M.; Christian, T.; Scandrett, C.; Norman, A. G.; Mascarenhas, A.; Misra, P.; Liu, T.; Sukiasyan, A.; Pickett, E.; Yuen, H. Doping dependence and anisotropy of minority electron mobility in molecular beam epitaxy-grown p type GaInP. *Appl. Phys. Lett.* **2014**, *105* (20), 202116, DOI: 10.1063/1.4902316

(52) Brenner, T. M.; Egger, D. A.; Rappe, A. M.; Kronik, L.; Hodes, G.; Cahen, D. Are Mobilities in Hybrid Organic-Inorganic Halide Perovskites Actually "High"? *J. Phys. Chem. Lett.* **2015**, *6* (23), 4754-4757, DOI: 10.1021/acs.jpclett.5b02390

(53) Im, J. H.; Jang, I. H.; Pellet, N.; Gratzel, M.; Park, N. G. Growth of CH3NH3PbI3 cuboids with controlled size for high-efficiency perovskite solar cells. *Nat. Nanotechnol.* **2014**, *9* (11), 927-932, DOI: 10.1038/nnano.2014.181

(54) Roebuck, B. Measurement of grain size and size distribution in engineering materials. *J. Mater. Sci. Technol.* **2000**, *16* (10), 1167-1174, DOI: 10.1179/026708300101506911

(55) Liu, Y.; Yang, Z.; Cui, D.; Ren, X.; Sun, J.; Liu, X.; Zhang, J.; Wei, Q.; Fan, H.; Yu, F.; et al. Two-Inch-Sized Perovskite CH3 NH3 PbX3 (X = Cl, Br, I) Crystals: Growth and Characterization. *Adv. Mater.* **2015**, *27* (35), 5176-5183, DOI: 10.1002/adma.201502597

(56) Wu, W. Q.; Wang, Q.; Fang, Y.; Shao, Y.; Tang, S.; Deng, Y.; Lu, H.; Liu, Y.; Li, T.; Yang, Z.; et al. Molecular doping enabled scalable blading of efficient hole-transport-layer-free perovskite solar cells. *Nat. Commun.* **2018**, *9* (1), 1625, DOI: 10.1038/s41467-018-04028-8

(57) Yang, S.; Chen, S.; Mosconi, E.; Fang, Y.; Xiao, X.; Wang, C.; Zhou, Y.; Yu, Z.; Zhao, J.; Gao, Y.; et al. Stabilizing halide perovskite surfaces for solar cell operation with wide-bandgap lead oxysalts. *Science* **2019**, *365* (6452), 473-478, DOI: 10.1126/science.aax3294

(58) Wu, W. Q.; Yang, Z.; Rudd, P. N.; Shao, Y.; Dai, X.; Wei, H.; Zhao, J.; Fang, Y.; Wang, Q.; Liu, Y.; et al. Bilateral alkylamine for suppressing charge recombination and improving stability in blade-coated perovskite solar cells. *Sci. Adv.* **2019**, *5* (3), eaav8925, DOI: 10.1126/sciadv.aav8925

(59) Liu, Z.; Park, J.-M.; Luo, L.; Cheng, D.; Huang, C.; Kim, R. H. J.; Vaswani, C.; Song, Z.; Yan, Y.; Yao, Y.; et al. Cryogenic spatial–temporal imaging of surface photocarrier dynamics in MAPbI3 films at the single grain level. *AIP Adv.* **2020**, *10* (12), 125108, DOI: 10.1063/5.0029022

(60) Zhang, W.; Pathak, S.; Sakai, N.; Stergiopoulos, T.; Nayak, P. K.; Noel, N. K.; Haghighirad, A. A.; Burlakov, V. M.; deQuilettes, D. W.; Sadhanala, A.; et al. Enhanced optoelectronic quality of perovskite thin films with hypophosphorous acid for planar heterojunction solar cells. *Nat. Commun.* **2015**, *6* (1), 10030, DOI: 10.1038/ncomms10030

(61) Wang, J. B.; Ding, D.; Johnson, S. R.; Yu, S. Q.; Zhang, Y. H. Determination and improvement of spontaneous emission quantum efficiency in GaAs/AlGaAs heterostructures grown by molecular beam epitaxy. *Phys. Status Solidi B* **2007**, *244* (8), 2740-2751, DOI: 10.1002/pssb.200675612

(62) Chen, Q.; Liu, H.; Kim, H.-S.; Liu, Y.; Yang, M.; Yue, N.; Ren, G.; Zhu, K.; Liu, S.; Park, N.-G.; et al. Erratum: Multiple-Stage Structure Transformation of Organic-Inorganic Hybrid Perovskite CH3NH3PbI3 [Phys. Rev. X 6, 031042 (2016)]. *Phys. Rev. X* **2017**, *7* (1), 019902, DOI: 10.1103/PhysRevX.7.019902

(63) Ferraro, J. R.; Nakamoto, K.; Brown, C. W. Analytical Chemistry. In *Introductory Raman Spectroscopy*, Ferraro, J. R., Nakamoto, K., Brown, C. W. Eds.; Academic Press, 2003; pp 267-293.

(64) Burwig, T.; Pistor, P. Reaction kinetics of the thermal decomposition of MAPbI3 thin films. *Phys. Rev. Mater.* **2021**, *5* (6), 065405, DOI: 10.1103/PhysRevMaterials.5.065405

(65) Bastos, J. P.; Uytterhoeven, G.; Qiu, W.; Paetzold, U. W.; Cheyns, D.; Surana, S.; Rivas, J.; Jaysankar, M.; Song, W.; Aernouts, T.; et al. Model for the Prediction of the Lifetime and Energy Yield of Methyl Ammonium Lead Iodide Perovskite Solar Cells at

Elevated Temperatures. *ACS Appl. Mater. Interfaces* **2019**, *11* (18), 16517-16526, DOI: 10.1021/acsami.9b00923

(66) Shirayama, M.; Kato, M.; Miyadera, T.; Sugita, T.; Fujiseki, T.; Hara, S.; Kadowaki, H.; Murata, D.; Chikamatsu, M.; Fujiwara, H. Degradation mechanism of CH3NH3PbI3 perovskite materials upon exposure to humid air. *J. Appl. Phys.* **2016**, *119* (11), 115501, DOI: 10.1063/1.4943638

(67) Pisoni, A.; Jacimovic, J.; Barisic, O. S.; Spina, M.; Gaal, R.; Forro, L.; Horvath, E. Ultra-Low Thermal Conductivity in Organic-Inorganic Hybrid Perovskite CH3NH3PbI3. *J. Phys. Chem. Lett.* **2014**, *5* (14), 2488-2492, DOI: 10.1021/jz5012109

(68) Niemann, R. G.; Kontos, A. G.; Palles, D.; Kamitsos, E. I.; Kaltzoglou, A.; Brivio, F.; Falaras, P.; Cameron, P. J. Halogen Effects on Ordering and Bonding of CH3NH3+ in CH3NH3PbX3 (X = Cl, Br, I) Hybrid Perovskites: A Vibrational Spectroscopic Study. *J. Phys. Chem. C* **2016**, *120* (5), 2509-2519, DOI: 10.1021/acs.jpcc.5b11256

(69) Sharma, R.; Dai, Z.; Gao, L.; Brenner, T. M.; Yadgarov, L.; Zhang, J.; Rakita, Y.; Korobko, R.; Rappe, A. M.; Yaffe, O. Elucidating the atomistic origin of anharmonicity in tetragonal CH3NH3PbI3 with Raman scattering. *Phys. Rev. Mater.* **2020**, *4* (9), 092401, DOI: 10.1103/PhysRevMaterials.4.092401

(70) Yaffe, O.; Guo, Y.; Tan, L. Z.; Egger, D. A.; Hull, T.; Stoumpos, C. C.; Zheng, F.; Heinz, T. F.; Kronik, L.; Kanatzidis, M. G.; et al. Local Polar Fluctuations in Lead Halide Perovskite Crystals. *Phys. Rev. Lett.* **2017**, *118* (13), 136001, DOI: 10.1103/PhysRevLett.118.136001

(71) Maalej, A.; Abid, Y.; Kallel, A.; Daoud, A.; Lautié, A.; Romain, F. Phase transitions and crystal dynamics in the cubic perovskite CH3NH3PbCl3. *Solid State Commun.* **1997**, *103* (5), 279-284, DOI: 10.1016/s0038-1098(97)00199-3

(72) Climent-Pascual, E.; Hames, B. C.; Moreno-Ramírez, J. S.; Álvarez, A. L.; Juarez-Perez, E. J.; Mas-Marza, E.; Mora-Seró, I.; de Andrés, A.; Coya, C. Influence of the substrate on the bulk properties of hybrid lead halide perovskite films. *J. Mater. Chem. A* **2016**, *4* (46), 18153-18163, DOI: 10.1039/c6ta08695k

(73) Ahn, N.; Kwak, K.; Jang, M. S.; Yoon, H.; Lee, B. Y.; Lee, J. K.; Pikhitsa, P. V.; Byun, J.; Choi, M. Trapped charge-driven degradation of perovskite solar cells. *Nat. Commun.* **2016**, *7* (1), 13422, DOI: 10.1038/ncomms13422

(74) Ni, Z.; Jiao, H.; Fei, C.; Gu, H.; Xu, S.; Yu, Z.; Yang, G.; Deng, Y.; Jiang, Q.; Liu, Y.; et al. Evolution of defects during the degradation of metal halide perovskite solar cells under reverse bias and illumination. *Nat. Energy* **2021**, *7* (1), 65-73, DOI: 10.1038/s41560-021-00949-9

(75) Liu, T.; Yue, S. Y.; Ratnasingham, S.; Degousee, T.; Varsini, P.; Briscoe, J.; McLachlan, M. A.; Hu, M.; Fenwick, O. Unusual Thermal Boundary Resistance in Halide Perovskites: A Way To Tune Ultralow Thermal Conductivity for Thermoelectrics. *ACS Appl. Mater. Interfaces* **2019**, *11* (50), 47507-47515, DOI: 10.1021/acsami.9b14174

(76) Khawam, A.; Flanagan, D. R. Solid-state kinetic models: basics and mathematical fundamentals. *J. Phys. Chem. B* **2006**, *110* (35), 17315-17328, DOI: 10.1021/jp062746a

(77) Ummadisingu, A.; Gratzel, M. Revealing the detailed path of sequential deposition for metal halide perovskite formation. *Sci. Adv.* **2018**, *4* (2), e1701402, DOI: 10.1126/sciadv.1701402

(78) Park, S. J.; Kim, A. R.; Hong, J. T.; Park, J. Y.; Lee, S.; Ahn, Y. H. Crystallization Kinetics of Lead Halide Perovskite Film Monitored by In Situ Terahertz Spectroscopy. *J. Phys. Chem. Lett.* **2017**, *8* (2), 401-406, DOI: 10.1021/acs.jpclett.6b02691

(79) Tran, C. D. T.; Liu, Y.; Thibau, E. S.; Llanos, A.; Lu, Z.-H. Stability of organometal perovskites with organic overlayers. *AIP Adv.* **2015**, *5* (8), 087185, DOI: 10.1063/1.4930082

(80) Sun, N. X.; Liu, X. D.; Lu, K. An explanation to the anomalous avrami exponent. *Scr. Mater.* **1996**, *34* (8), 1201-1207, DOI: 10.1016/1359-6462(95)00657-5

(81) Haye, E.; Capon, F.; Barrat, S.; Boulet, P.; Andre, E.; Carteret, C.; Bruyere, S. Properties of rare-earth orthoferrites perovskite driven by steric hindrance. *J. Alloys Compd.* **2016**, *657*, 631-638, DOI: 10.1016/j.jallcom.2015.10.135

(82) Różycki, C.; Maciejewski, M. Method of the selection of the g(α) function based on the reduced-time plot. *Thermochim. Acta* **1987**, *122* (2), 339-354, DOI: 10.1016/0040-6031(87)87052-1

(83) Pang, E. L.; Vo, N. Q.; Philippe, T.; Voorhees, P. W. Modeling interface-controlled phase transformation kinetics in thin films. *J. Appl. Phys.* **2015**, *117* (17), DOI: 10.1063/1.4919725

(84) Očenášek, J.; Novák, P.; Agbo, S. Finite-thickness effect on crystallization kinetics in thin films and its adaptation in the Johnson–Mehl–Avrami–Kolmogorov model. *J. Appl. Phys.* **2014**, *115* (4), 043505, DOI: 10.1063/1.4862858

(85) Chen, B.; Song, J.; Dai, X.; Liu, Y.; Rudd, P. N.; Hong, X.; Huang, J. Synergistic Effect of Elevated Device Temperature and Excess Charge Carriers on the Rapid Light-

Induced Degradation of Perovskite Solar Cells. *Adv. Mater.* **2019**, *31* (35), e1902413, DOI: 10.1002/adma.201902413

(86) Meggiolaro, D.; Mosconi, E.; De Angelis, F. Modeling the Interaction of Molecular Iodine with MAPbI3: A Probe of Lead-Halide Perovskites Defect Chemistry. *ACS Energy Lett.* **2018**, *3* (2), 447-451, DOI: 10.1021/acsenergylett.7b01244

(87) Ye, T.; Kocherga, M.; Sun, Y. Y.; Nesmelov, A.; Zhang, F.; Oh, W.; Huang, X. Y.; Li, J.; Beasock, D.; Jones, D. S.; et al. II-VI Organic-Inorganic Hybrid Nanostructures with Greatly Enhanced Optoelectronic Properties, Perfectly Ordered Structures, and Shelf Stability of Over 15 Years. *ACS Nano* **2021**, *15* (6), 10565-10576, DOI: 10.1021/acsnano.1c03219

(88) Udalova, N. N.; Tutantsev, A. S.; Chen, Q.; Kraskov, A.; Goodilin, E. A.; Tarasov, A. B. New Features of Photochemical Decomposition of Hybrid Lead Halide Perovskites by Laser Irradiation. *ACS Appl. Mater. Interfaces* **2020**, *12* (11), 12755-12762, DOI: 10.1021/acsami.9b21689

(89) Petrov, A. A.; Belich, N. A.; Grishko, A. Y.; Stepanov, N. M.; Dorofeev, S. G.; Maksimov, E. G.; Shevelkov, A. V.; Zakeeruddin, S. M.; Graetzel, M.; Tarasov, A. B.; et al. A new formation strategy of hybrid perovskites via room temperature reactive polyiodide melts. *Mater. Horiz.* **2017**, *4* (4), 625-632, DOI: 10.1039/c7mh00201g

(90) Wu, X.; Tan, L. Z.; Shen, X.; Hu, T.; Miyata, K.; Trinh, M. T.; Li, R.; Coffee, R.; Liu, S.; Egger, D. A.; et al. Light-induced picosecond rotational disordering of the inorganic sublattice in hybrid perovskites. *Sci. Adv.* **2017**, *3* (7), e1602388, DOI: 10.1126/sciadv.1602388

(91) Park, M.; Kornienko, N.; Reyes-Lillo, S. E.; Lai, M.; Neaton, J. B.; Yang, P.; Mathies, R. A. Critical Role of Methylammonium Librational Motion in Methylammonium Lead Iodide (CH3NH3PbI3) Perovskite Photochemistry. *Nano Lett.* **2017**, *17* (7), 4151-4157, DOI: 10.1021/acs.nanolett.7b00919

(92) Son, D.-Y.; Lee, J.-W.; Choi, Y. J.; Jang, I.-H.; Lee, S.; Yoo, P. J.; Shin, H.; Ahn, N.; Choi, M.; Kim, D.; et al. Self-formed grain boundary healing layer for highly efficient CH3NH3PbI3 perovskite solar cells. *Nat. Energy* **2016**, *1* (7), 16081, DOI: 10.1038/nenergy.2016.81

(93) Zhou, Y.; You, L.; Wang, S.; Ku, Z.; Fan, H.; Schmidt, D.; Rusydi, A.; Chang, L.; Wang, L.; Ren, P.; et al. Giant photostriction in organic-inorganic lead halide perovskites. *Nat. Commun.* **2016**, *7* (1), 11193, DOI: 10.1038/ncomms11193

(94) Lin, Y.; Chen, B.; Fang, Y.; Zhao, J.; Bao, C.; Yu, Z.; Deng, Y.; Rudd, P. N.; Yan, Y.; Yuan, Y.; et al. Excess charge-carrier induced instability of hybrid perovskites. *Nat. Commun.* **2018**, *9* (1), 4981, DOI: 10.1038/s41467-018-07438-w

(95) Righetto, M.; Lim, S. S.; Giovanni, D.; Lim, J. W. M.; Zhang, Q.; Ramesh, S.; Tay, Y. K. E.; Sum, T. C. Hot carriers perspective on the nature of traps in perovskites. *Nat. Commun.* **2020**, *11* (1), 2712, DOI: 10.1038/s41467-020-16463-7

(96) Gfroerer, T. H.; Zhang, Y.; Wanlass, M. W. An extended defect as a sensor for free carrier diffusion in a semiconductor. *Appl. Phys. Lett.* **2013**, *102* (1), DOI: 10.1063/1.4775369

(97) Sajedi Alvar, M.; Blom, P. W. M.; Wetzelaer, G. A. H. Space-charge-limited electron and hole currents in hybrid organic-inorganic perovskites. *Nat. Commun.* **2020**, *11* (1), 4023, DOI: 10.1038/s41467-020-17868-0

(98) Zhang, Y.; Sturge, M. D.; Kash, K.; van der Gaag, B. P.; Gozdz, A. S.; Florez, L. T.; Harbison, J. P. Temperature dependence of luminescence efficiency, exciton transfer, and exciton localization in GaAs/AlxGa1-xAs quantum wires and quantum dots. *Phys. Rev. B: Condens.* **1995**, *51* (19), 13303-13314, DOI: 10.1103/physrevb.51.13303

(99) Gfroerer, T. H. Photoluminescence in Analysis of Surfaces and Interfaces. In *Encyclopedia of Analytical Chemistry*, 2006.

(100) Draguta, S.; Thakur, S.; Morozov, Y. V.; Wang, Y.; Manser, J. S.; Kamat, P. V.; Kuno, M. Spatially Non-uniform Trap State Densities in Solution-Processed Hybrid Perovskite Thin Films. *J. Phys. Chem. Lett.* **2016**, *7* (4), 715-721, DOI: 10.1021/acs.jpclett.5b02888

(101) Zhang, F.; Castaneda, J. F.; Gfroerer, T. H.; Friedman, D.; Zhang, Y. H.; Wanlass, M. W.; Zhang, Y. An all optical approach for comprehensive in-operando analysis of radiative and nonradiative recombination processes in GaAs double heterostructures. *Light Sci. Appl.* **2022**, *11* (1), 137, DOI: 10.1038/s41377-022-00833-5

(102) Phung, N.; Mattoni, A.; Smith, J. A.; Skroblin, D.; Köbler, H.; Choubrac, L.; Breternitz, J.; Li, J.; Unold, T.; Schorr, S.; et al. Photoprotection in metal halide perovskites by ionic defect formation. *Joule* **2022**, *6* (9), 2152-2174, DOI: 10.1016/j.joule.2022.06.029

(103) Bi, Y.; Hutter, E. M.; Fang, Y.; Dong, Q.; Huang, J.; Savenije, T. J. Charge Carrier Lifetimes Exceeding 15 mus in Methylammonium Lead Iodide Single Crystals. *J. Phys. Chem. Lett.* **2016**, *7* (5), 923-928, DOI: 10.1021/acs.jpclett.6b00269

(104) Guo, D.; Bartesaghi, D.; Wei, H.; Hutter, E. M.; Huang, J.; Savenije, T. J. Photoluminescence from Radiative Surface States and Excitons in Methylammonium

Lead Bromide Perovskites. *J. Phys. Chem. Lett.* **2017**, *8* (17), 4258-4263, DOI: 10.1021/acs.jpclett.7b01642

(105) Xing, J.; Zou, Y.; Zhao, C.; Yu, Z.; Shan, Y.; Kong, W.; Zheng, X.; Li, X.; Yu, W.; Guo, C. Thickness-dependent carrier lifetime and mobility for MAPbBr3 single crystals. *Mater. Today Phys.* **2020**, *14*, 100240, DOI: 10.1016/j.mtphys.2020.100240

(106) Schnitzer, I.; Yablonovitch, E.; Caneau, C.; Gmitter, T. J. Ultrahigh spontaneous emission quantum efficiency, 99.7% internally and 72% externally, from AlGaAs/GaAs/AlGaAs double heterostructures. *Appl. Phys. Lett.* **1993**, *62* (2), 131-133, DOI: 10.1063/1.109348

(107) Pazos-Outon, L. M.; Szumilo, M.; Lamboll, R.; Richter, J. M.; Crespo-Quesada, M.; Abdi-Jalebi, M.; Beeson, H. J.; Vrucinic, M.; Alsari, M.; Snaith, H. J.; et al. Photon recycling in lead iodide perovskite solar cells. *Science* **2016**, *351* (6280), 1430-1433, DOI: 10.1126/science.aaf1168

(108) Kayes, B. M.; Nie, H.; Twist, R.; Spruytte, S. G.; Reinhardt, F.; Kizilyalli, I. C.; Higashi, G. S. 27.6% Conversion efficiency, a new record for single-junction solar cells under 1 sun illumination. *2011 37th IEEE Photovoltaic Specialists Conference* **2011**, 000004-000008,

(109) Raja, W.; De Bastiani, M.; Allen, T. G.; Aydin, E.; Razzaq, A.; Rehman, A. u.; Ugur, E.; Babayigit, A.; Subbiah, A. S.; Isikgor, F. H.; et al. Photon recycling in perovskite solar cells and its impact on device design. *Nanophotonics* **2021**, *10* (8), 2023-2042, DOI: 10.1515/nanoph-2021-0067

(110) Fassl, P.; Lami, V.; Berger, F. J.; Falk, L. M.; Zaumseil, J.; Richards, B. S.; Howard, I. A.; Vaynzof, Y.; Paetzold, U. W. Revealing the internal luminescence

quantum efficiency of perovskite films via accurate quantification of photon recycling. *Matter* **2021**, *4* (4), 1391-1412, DOI: 10.1016/j.matt.2021.01.019

(111) Xiao, R.; Hou, Y.; Fu, Y.; Peng, X.; Wang, Q.; Gonzalez, E.; Jin, S.; Yu, D. Photocurrent Mapping in Single-Crystal Methylammonium Lead Iodide Perovskite Nanostructures. *Nano Lett.* **2016**, *16* (12), 7710-7717, DOI: 10.1021/acs.nanolett.6b03782

(112) Liu, S.; Wang, L.; Lin, W. C.; Sucharitakul, S.; Burda, C.; Gao, X. P. Imaging the Long Transport Lengths of Photo-generated Carriers in Oriented Perovskite Films. *Nano Lett.* **2016**, *16* (12), 7925-7929, DOI: 10.1021/acs.nanolett.6b04235

(113) Chen, Y. F.; Tsai, Y. T.; Bassani, D. M.; Clerc, R.; Forgács, D.; Bolink, H. J.; Wussler, M.; Jaegermann, W.; Wantz, G.; Hirsch, L. Evidence of band bending induced by hole trapping at MAPbI3perovskite/metal interface. *J. Mater. Chem. A* **2016**, *4* (44), 17529-17536, DOI: 10.1039/c6ta08979h

(114) Hu, X.; Wang, X.; Fan, P.; Li, Y.; Zhang, X.; Liu, Q.; Zheng, W.; Xu, G.; Wang, X.; Zhu, X.; et al. Visualizing Carrier Transport in Metal Halide Perovskite Nanoplates via Electric Field Modulated Photoluminescence Imaging. *Nano Lett.* **2018**, *18* (5), 3024-3031, DOI: 10.1021/acs.nanolett.8b00486

(115) Mott, N.; Gurney, R. *Electronic Processes in Ionic Crystals*; Oxford University Press, 1940.

(116) Chen, Q.; McKeon, B. S.; Zhang, S. Y.; Zhang, F.; Hu, C.; Gfroerer, T. H.; Wanlass, M. W.; Smith, D. J.; Zhang, Y. Impact of Individual Structural Defects in GaAs Solar Cells: A Correlative and In Operando Investigation of Signatures, Structures, and Effects. *Adv. Opt. Mater.* **2020**, *9* (2), 2001487, DOI: 10.1002/adom.202001487